Dissociation between catecholamines and acetylcholine in the human cerebral cortex

Authors: T. Pfeffer[1,2]*, A. Ponce-Alvarez[2], T. Meindertsma[1,3], C. Gahnström[1], R. L. van den Brink[1], G. Nolte[1], K. Tsetsos[1], A.K. Engel[1], G. Deco[2,4,5,6], T.H. Donner[1,3,7,8]*

Affiliations:
[1]Department of Neurophysiology and Pathophysiology, University Medical Center Hamburg-Eppendorf, Germany.
[2]Center for Brain and Cognition, Computational Neuroscience Group, Universitat Pompeu Fabra, Barcelona, Spain
[3]Department of Psychology, University of Amsterdam, The Netherlands.
[4]Institució Catalana de la Recerca i Estudis Avançats (ICREA), Barcelona, Spain
[5]Department of Neuropsychology, Max Planck Institute for Human Cognitive and Brain Sciences, Leipzig, Germany
[6]School of Psychological Sciences, Monash University, Melbourne, Australia
[7]Amsterdam Brain and Cognition, University of Amsterdam, The Netherlands.
[8]Bernstein Center for Computational Neuroscience Berlin, Germany.

*Correspondence to: thms.pfffr@gmail.com, t.donner@uke.de

Abstract:

The catecholamine and acetylcholine systems control global brain states. Influential theoretical accounts postulate distinct computational roles of these systems. But previous empirical work observed only subtle, quantitative differences between their effects on single-neuron responses in the cortex. Here, we report a double dissociation between catecholamine and acetylcholine effects on large-scale cortical dynamics in humans. A pharmacological boost of catecholamine levels increased the cortex-wide coupling between regional fluctuations of population activity during a visual task. In contrast, a pharmacological acetylcholine boost decreased coupling during rest. Circuit modeling explained these results by distinct changes in local cortical circuit properties (specifically, excitation/inhibition balance) and predicted that catecholamines would promote more exploratory choice behavior. Indeed, we observed increased exploration under catecholamine boost in two behavioral tasks. We conclude that distinct local circuit mechanisms cause dissociated context-dependent catecholamine and acetylcholine effects on large-scale cortical dynamics.

Introduction

The catecholaminergic (noradrenergic and dopaminergic) and cholinergic modulatory systems of the brainstem regulate the state of the cortical networks underlying cognition (*1–4*). The noradrenergic and cholinergic systems have similar connectivity with the cerebral cortex, sending ascending projections to the entire cortex and receiving descending projections from prefrontal regions (*1*, *5*, *6*). Noradrenaline, dopamine, and acetylcholine all increase the responsivity ('gain') of cortical neurons to synaptic input (*1*, *7–9*). Despite these qualitatively similar architectures and single-cell physiological effects, influential theoretical accounts postulate distinct computational roles of the catecholamine and acetylcholine systems in cognition and behavior (*1*, *10*, *11*). Thus, these neuromodulators should have qualitatively distinct effects on the cortical population dynamics that mediate cognition. Indeed, computational modeling shows that the brain-wide interaction of subtle local microcircuit effects can give rise to profound qualitative effects at the level of large-scale cortical networks (*12*).

Here, we report a behavioral context-dependent double dissociation between catecholaminergic and cholinergic effects on large-scale cortical network dynamics (Fig. 1). We increased central catecholamine and acetylcholine levels in healthy human participants through the placebo-controlled administration of atomoxetine and donepezil, respectively (Fig. 1A, left; Materials and Methods). Atomoxetine is a selective noradrenaline reuptake inhibitor, which boosts noradrenaline levels across cortex (*13*). Atomoxetine also increases dopamine levels in its more restricted cortical projection targets including prefrontal cortex (*14*). Donepezil is a cholinesterase inhibitor (*15*).

Atomoxetine, but not donepezil, increased pupil size (Fig. 1B, Fig. S1), a peripheral marker of central arousal state (*5*). We measured the effects of these interventions on cortical activity with whole-head magnetoencephalography (MEG) in two behavioral contexts: a visual task with continuous input and eyes-open 'rest' (Fig. 1A, right). The task entailed the continuous presentation of an ambiguous visual stimulus, which, in turn, induced spontaneous and ongoing alternations in perception ((*16*); Movie S1). During MEG blocks, we asked participants to silently count the perceptual alternations, so that we could assess intrinsic fluctuations in MEG activity in the absence of transients in visual input and motor movements. In separate blocks, participants reported each perceived alternation with an immediate button press.

Distinct context-dependent drug effects on cortex-wide network dynamics

Large-scale cortical population dynamics were quantified as the frequency-resolved, cortex-wide correlations of intrinsic activity fluctuations during both 'steady-state' behavioral contexts (Fig. S2A). We computed pairwise correlations between 400 cortical locations and compiled them into a matrix, separately for a range of frequencies. Averaged across the placebo-rest condition, this yielded a similar spatial and spectral structure of correlations as previously reported (*17*) (Fig. S2B,C). We then statistically compared the correlation matrices (Fig. S3) of each drug condition with the correlation matrices of the placebo condition (Fig. S4) and computed the fraction of significantly increased and decreased correlations (Materials and Methods).

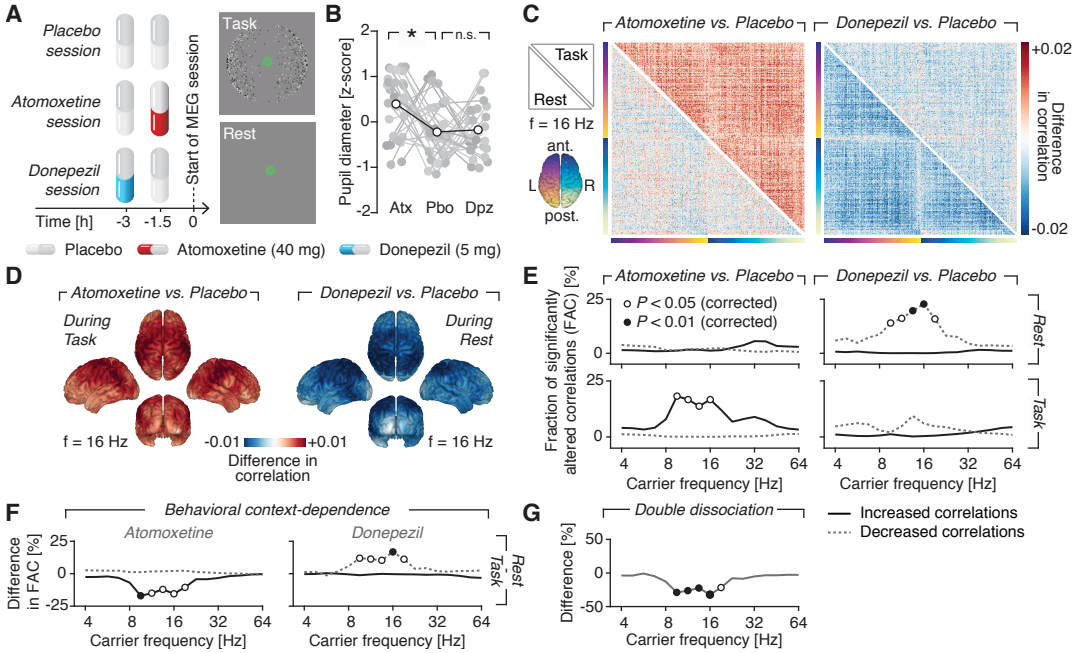

Fig. 1. Dissociated catecholaminergic and cholinergic effects on cortex-wide correlations in activity. (A) Experimental design. Top: Atomoxetine (40 mg), donepezil (5 mg), or a visually indistinguishable placebo was administered before each session. Bottom: MEG activity was recorded during a visual task (left) or eyes-open 'rest' (right). **(B)** Drug effect on baseline pupil diameter (rest and task collapsed. Atx, atomoxetine; Pbo, placebo; Dpz, donepezil; * $P < 0.05$, paired two-sided permutation test) **(C)** Drug effects on cortex-wide activity correlations (at 16 Hz), for task (upper triangle) and rest (lower triangle). Left: atomoxetine – placebo; Right: donepezil – placebo. **(D)** Cortical distribution of drug effects on correlations. Left: Atomoxetine – placebo (task). Right: Donepezil – placebo (rest). **(E)** Frequency spectrum of drug effects on the fraction of significantly (P<0.05, paired t-test) altered correlations across brain regions, for atomoxetine (left) and donepezil (left) as well as for rest (top) and task (bottom). Fractions of significantly increased (solid black lines) and decreased (dashed gray lines) correlations are shown separately. **(F)** Effect of behavioral context on correlations (difference between upper and lower rows in E). **(G)** Spectrum of double dissociation (difference between solid black line in left column of panel E and dashed gray line in right column of panel E). Open circles, $P < 0.05$; filled circles, $P < 0.01$ (paired two-sided single-threshold permutation test).

Atomoxetine (catecholamines) increased correlations across most pairs of regions during task (Fig. 1C, left; upper triangular part; Fig. S4A). This effect was evident in all four cerebral lobes (Fig. 1D, left) and peaked in the 'alpha/beta' frequency band (9.51-16 Hz; Fig. 1E, left). The effect was absent during rest (Fig. 1E; upper vs. lower triangular part in Fig. 1C). In sharp contrast, donepezil (acetylcholine) decreased correlations across most region pairs, but only during rest (Fig. 1C, right, lower triangular part; Fig. 1E, right; Fig. S4B). Thus, both drugs had opposite context-dependent effects on correlations (Fig. 1F), yielding a frequency-specific double dissociation (Fig. 1G; all P-values < 0.01 for the range: 9.51-16 Hz).

The double dissociation between the drug effects was neither present at the level of local activity fluctuations ((*18*) and Fig. S5), nor did it depended on specific choices of analysis parameters (Fig. S6-7).

Large-scale drug effects can be explained by distinct changes in local circuit parameters

Catecholamines and acetylcholine both increase the gain of cortical neurons (*1*, *7–9*). How, then, did the dissociation between their large-scale effects arise? To illuminate this question, we modeled the mass activity of coupled cortical regions ('nodes'), each of which was composed of an interconnected excitatory and inhibitory neural population (Fig. 2A, B) (*19*). The model had four free parameters: the background inputs to excitatory (b_E) and inhibitory (b_I) populations, the

slope of the input-output function ('gain' at the neural population level) and a global coupling parameter (Materials and Methods). Our modeling was guided by two assumptions: First, we assumed that cortical mass activity exhibits noise-driven oscillations, as opposed to sustained oscillations. Second, we assumed increased background input (b) to excitatory populations (b_E) and inhibitory populations (b_I) in many cortical regions during task (*20*). Correspondingly, in the model, task increased the background input to excitatory as well as inhibitory populations relative to rest, resulting in an upward-rightward shift in the (b_E, b_I)-plane. Fig. 2C illustrates these two assumptions for a version of the model made up of only two nodes in terms of the gray shaded area (top left; sustained oscillations) and the dashed black outline (task-related increase in background input). These assumptions were derived from established cortical physiology (Supplementary text) and enabled us to test the hypothesis that differences in gain modulation and/or changes in global coupling could explain the double dissociation observed in the data.

An increase in gain was sufficient to explain the context-dependent effect of atomoxetine on cortical correlations (Fig. 2C). Just as observed in the empirical data (Fig. 1E, left), increasing the gain in the 'two-node model' produced distinct changes in correlations for different contexts situated in the (b_E, b_I)-plane (i.e., different levels of background drive; rest: white circle; task: yellow circle; Fig. 2C). In a realistic model of the whole cortex (Fig. 2B, right), which was fitted to the measured correlation matrix for rest-placebo (Fig. S8F), gain increase boosted correlations in the same context-dependent fashion, with no change at rest (Fig. 2D, light gray circle or bar), but a robust increase during task (Fig. 2D, yellow circle or bar).

The model could also explain the opposite, context-dependent effect of acetylcholine (Fig. 1E, right): an increase in gain (smaller than the catecholaminergic one, see below) combined with a decrease in the model's global coupling parameter resulted in decreased correlations during rest, but not during task (Fig. 2E). Decreased global coupling is in line with a reduction of intracortical (lateral and/or feedback) signaling in visual and auditory cortex (*15*, *21*, *22*) and perception (*23*), possibly mediated by muscarinic receptors (*22*).

Changes in neural gain result from complex synaptic interactions within cortical microcircuits (*24*). We reasoned that the catecholaminergic increase in the gain in our large-scale circuit model may have emerged from an increase in the ratio between excitation and inhibition (henceforth termed 'E/I') of local synaptic interactions (*9*, *25*, *26*). We tested this hypothesis through simulation of a conductance-based cortical microcircuit model made up of recurrently connected excitatory and inhibitory spiking neurons (Materials and Methods; Fig. 2F, top; Fig. S10). Consistent with single neuron simulations (*26*), increasing the circuit's E/I (decreasing the strength of feedback inhibition) indeed boosted the response gain of the input-output function of the excitatory cells (Fig. 2F, bottom) also in this population of spiking neurons.

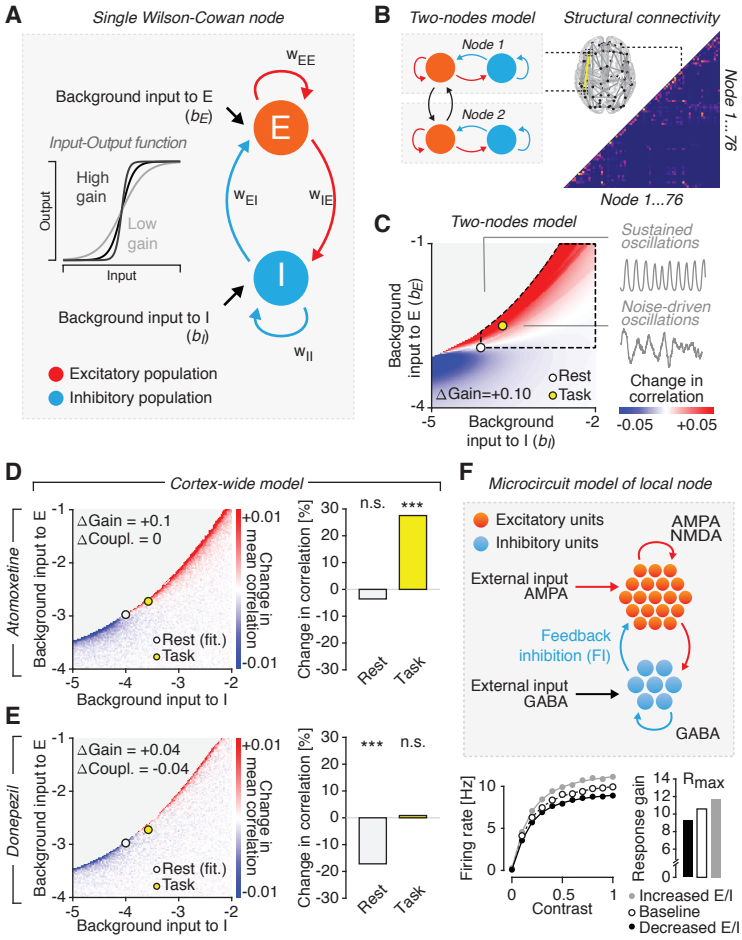

Fig. 2. Circuit mechanisms of context-dependent effects on cortex-wide correlations. (A) Schematic of a single node (brain region) consisting of an excitatory (E) and an inhibitory population (I), with full connectivity and independent background input to E and I (Wilson-Cowan model (*19*)). Inset, input-output function of each population for various gain parameters (slope of the input-output function). **(B)** Left: Correlations were computed between the firing rates of the E populations of two or more nodes. Right: For the cortex-wide model, an estimate of the human structural connectome was used to connect a total of 76 nodes, and the model was fitted to the rest-placebo data (Materials and Methods). **(C)** Change in correlation under an increase in gain (+0.1) in the (b_E, b_I)-plane of the 'two-nodes model'. Inset: sustained and noise-driven oscillations. The area defined by the dashed black line highlights the assumed task-related shift in the (b_E, b_I)-plane. **(D)** Effect of gain increase (+0.1) across all 76x76 node pairs (right; white circle: rest; yellow circle: task) **(E)** As D, but for donepezil with gain increase by +0.04 (see Fig. S9 for +0.1) and decrease in global coupling (-0.04). **(F)** Top: Architecture of microcircuit consisting of excitatory and inhibitory integrate-and-fire neurons (all-to-all connectivity). Bottom, left: Effect of change in E/I (feedback inhibition) on gain for increases (decreased E/I; black line; filled black circles) and decreases in feedback inhibition (increased E/I; gray line; filled gray circles), with respect to baseline (dashed line; open circles). Bottom, right: fitted response gain parameter (R_{max}) of the stimulus-response function (Materials and Methods) for three levels of E/I.

Inferred circuit-level mechanism also accounts for changes in behavior

Increasing catecholamine levels, and cortical E/I, also rendered selection behavior more variable (Fig. 3). Atomoxetine (not donepezil) increased the number of perceptual alternations reported by participants (Fig. 3A), an effect not due to a change in eye movements or blinks (*18*). This effect was evident both when participants silently counted the perceptual transitions and when they reported each perceptual transitions with an immediate button press (Fig. S12). To make the microcircuit model produce selection behavior, we expanded it by means of two populations of excitatory neurons encoding a specific decision ('D1' and 'D2'), which competed via feedback

inhibition (*27*) (Fig. 3B, left; Fig. S11). Increasing E/I in this model has been shown to yield more variable decision-making in standard two-alternative forced choice tasks (*28*). To model our current task, we simulated the model under sustained, and equally strong, input to D1 and D2, modelling unbiased competition. Just as our participants under atomoxetine, the model exhibited ongoing alternations in the activity dominance of D1 or D2 (Fig. S11B) and an increase in the alternation rate under increased E/I due to decreased feedback inhibition (Fig. 3B, right). In other words, participants, as well as the model, were more prone to 'explore' different perceptual interpretations of a constant, ambiguous input.

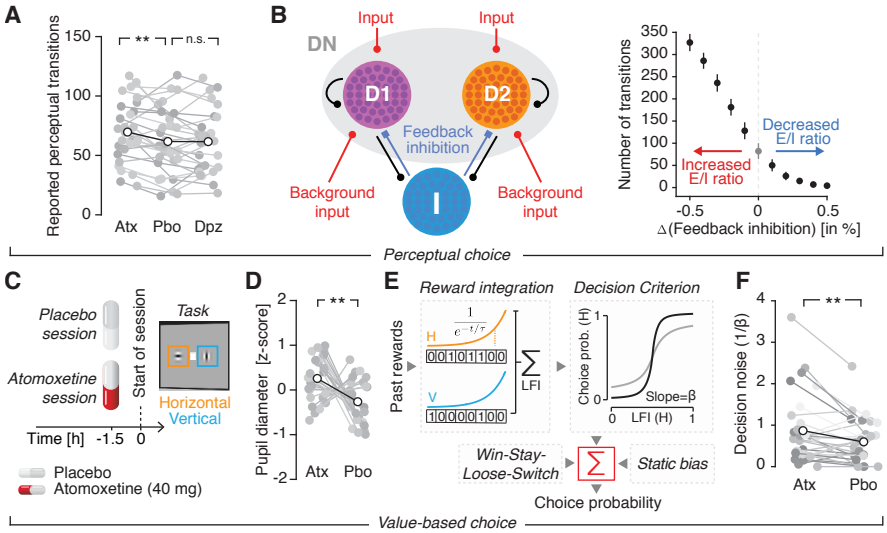

Fig. 3. Catecholamine-induced increase in E/I ratio can promote behavioral exploration. (A) Effect of atomoxetine on rate of alternations in the judgment of continuous input (changes in the apparent direction of rotation of the seemingly rotating sphere). **(B)** Left: Schematic of the decision circuit, endowed with two excitatory decision populations, D1 and D2, and a non-selective population (DN), fully connected to a pool of inhibitory neurons. The two decision populations receive noisy Poisson input, reflecting the ambiguous nature of the visual stimulus. Right: Effect of E/I increase in circuit model on rate of alternations in the judgment of continuous input. E/I increase in the circuit model is implemented via decrease in feedback inhibition (red/blue arrows) **(C)** Administration protocol for the value-based choice experiment: atomoxetine (40 mg) or a visually indistinguishable placebo was administered before each session **(D)** Effect of atomoxetine on baseline pupil diameter **(E)** Schematic of the algorithmic model for value-based choice task (dynamic foraging). Choice behavior was analyzed with a reward integration model consisting of four parameters: integrator leak, decision noise (1/β of softmax transformation), weight of 'win-stay, loose-switch' heuristic, overall (static) bias (Materials and Methods). **(F)** Effect of atomoxetine on the decision noise parameter. The other three model parameters showed no clear effect (Fig. S13G).

An influential view holds that catecholamines render decision-making exploratory when required by the behavioral context, e.g. during foraging (*1*). We, thus, performed a second behavioral experiment to probe the effect of atomoxetine (same dose as for perceptual task, Fig. 3C) on decision-making during a version of a foraging task previously used in monkeys (*29*). Atomoxetine again increased baseline pupil diameter (Fig. 3D). On each trial, participants chose between two target stimuli (horizontal/vertical Gabor patches, Fig. S13A) associated with different reward histories (Fig. S13A-C; Materials and Methods). We fitted behavior with an algorithmic model made up of four parameters that could differ between atomoxetine and placebo (Fig. 3E). The 'decision noise' (1/β) parameter, governing choice variability, selectively increased under atomoxetine (Fig. 3F). This effect on decision noise was independent of the encoding and temporal integration of rewards, which are commonly linked to the dopamine system (*11*). The latter were quantified by the leak (inverse of integration time constant τ, see Fig. 3E), for which we observed no effect (Fig. S13). The finding of increased decision noise is in line with the circuit model

prediction for E/I increase (*28*). In sum, elevated catecholamine levels increased behavioral exploration in sensory- and value-guided behavior, likely via increasing E/I in cortical circuits.

Discussion

Previous animal work has reported differences between noradrenaline and acetylcholine effects on the firing rates or membrane potential fluctuations of single neurons (*9*, *30*), but not a qualitative double dissociation like the one we observed here. Our model shows that subtle differences of catecholamine and acetylcholine effects at the cellular level (e.g. gain increases of different magnitude (*1*, *7*, *8*)) can combine to yield context-dependent (here: task vs. rest) dissociations at the level of large-scale cortical network dynamics. This can account for the double dissociation between neuromodulator effects reported here, and help reconcile different findings reported in the pharmacological neuroimaging literature (Supplementary Text).

Our model-based inference that both modulators increase overall gain (and hence E/I), but with different magnitudes, is largely consistent with single-cell physiology (*1*, *8*, *20*, *25*, *31*). Specifically, noradrenaline and acetylcholine both increase E/I in rodent auditory cortex by decreasing inhibitory inputs to pyramidal cells, but in different ways (*25*): Acetylcholine suppresses phasic, stimulus-evoked inhibition (*32*, *33*), whereas noradrenaline decreases tonic, ongoing inhibition (*31*). Further, longer-lasting, plastic changes of cortical stimulus responses induced by neuromodulators are more indiscriminate under noradrenaline (affecting all neurons in the circuit regardless of tuning), while they are selective for stimulus-responsive neurons under acetylcholine (*25*, *32*). Such differences at the synaptic and cellular levels might translate into the difference in gain increase in our neural mass model under the two drugs, with a subtler gain increase under acetylcholine (Supplementary Text).

Our second inference, of reduced intra-cortical communication (global coupling) under acetylcholine, is also consistent with physiological data from sensory cortex (*15*, *21*, *22*). It also aligns well with accounts of probabilistic inference, which assume that acetylcholine reduces the impact of prior knowledge (intra-cortical signaling) relative to incoming evidence (bottom-up signaling; Supplementary Text) (*10*). However, evidence from prefrontal cortex suggests that acetylcholine can also increase synaptic efficacy on recurrent intra-cortical connections, through both nicotinic and muscarinic receptors (*34*). Further work is needed to elucidate the synaptic basis of the cholinergic effects observed here.

Our behavioral results confirm a key prediction from an influential account of the role of the noradrenaline system in the regulation of the exploration-exploitation tradeoff (*1*). In this view, high tonic noradrenaline levels boost behavioral variability. While this is detrimental to performance in static environments, it is adaptive in the presence of hidden environmental changes, as were present in our foraging task (Materials and Methods), by promoting exploration of alternatives (*1*, *35*, *36*). Indeed, animal behavior becomes more variable during periods of high tonic firing of the locus coeruleus in perceptual tasks in static environments (*35*, *37*) as well in value-based choice in changing environments (*38*, *39*) – specifically, an increase of decision noise during rat foraging behavior (*38*). These findings in animals are in line with our current results in humans (Supplementary Text).

Our results may establish a physiological basis for the distinct roles of catecholamines and acetylcholine in cognition postulated by computational theories (*1*, *10*). One prominent idea holds that the noradrenaline and acetylcholine systems track two forms of uncertainty during inference in natural environments: Acetylcholine signals so-called ‘expected uncertainty’, which originates

from the inherent noise corrupting the information received in a given (constant) state of the environment; noradrenaline signals 'unexpected uncertainty', stemming from hidden changes in the state of the environment (*10*). These two forms of uncertainty should have separable influences on the neural computations in the cortex that underlie inference. Our results suggest that such functional distinction may be mediated by differential modulatory effects on local and large-scale cortical circuits.

Intrinsic correlations in brain activity are widely used in basic human neuroscience and clinical biomarker development (*12*, *17*, *40*). The behavioral context-dependence of the neuromodulatory effects we uncovered here implies that resting-state measurements alone lack a critical dimension: the comparison between rest and task contexts was necessary to uncover the specific impact of neuromodulators on cortical dynamics. It is likely that the same holds for other classes of neurotransmitters, and their disturbances in brain disorders. Our approach sets the stage for the development of new non-invasive assessments of the integrity of neuromodulatory systems.

References and Notes:

1. G. Aston-Jones, J. D. Cohen, *Annu. Rev. Neurosci.* **28**, 403–450 (2005).
2. K. D. Harris, A. Thiele, *Nat. Rev. Neurosci.* **12**, 509–523 (2011).
3. A. F. T. Arnsten, *Nat Neurosci*. **18**, 1376–1385 (2015).
4. M. F. Bear, W. Singer, *Nature*. **320**, 172–176 (1986).
5. V. Breton-Provencher, M. Sur, *Nat Neurosci*. **22**, 218–228 (2019).
6. L. A. Schwarz, L. Luo, *Current Biology*. **25**, R1051–R1056 (2015).
7. D. Servan-Schreiber, H. Printz, J. Cohen, *Science*. **249**, 892–895 (1990).
8. J. L. Herrero *et al.*, *Nature*. **454**, 1110–1114 (2008).
9. P.-O. Polack, J. Friedman, P. Golshani, *Nat. Neurosci.* **16**, 1331–1339 (2013).
10. A. J. Yu, P. Dayan, *Neuron*. **46**, 681–692 (2005).
11. P. R. Montague, S. E. Hyman, J. D. Cohen, *Nature*. **431**, 760–767 (2004).
12. G. Deco *et al.*, *J. Neurosci.* **34**, 7886–7898 (2014).
13. T. W. Robbins, A. F. T. Arnsten, *Annu. Rev. Neurosci.* **32**, 267–287 (2009).
14. F. P. Bymaster *et al.*, *Neuropsychopharmacology*. **27**, 699–711 (2002).
15. M. A. Silver, A. Shenhav, M. D'Esposito, *Neuron*. **60**, 904–914 (2008).
16. D. Leopold, N. Logothetis, **3**, 254–264 (1999).
17. J. F. Hipp, D. J. Hawellek, M. Corbetta, M. Siegel, A. K. Engel, *Nature Neuroscience*. **15**, 884–890 (2012).
18. T. Pfeffer *et al.*, *PLOS Biology*. **16**, e2003453 (2018).
19. H. R. Wilson, J. D. Cowan, *Biophysical Journal*. **12**, 1–24 (1972).
20. B. Haider, M. Häusser, M. Carandini, *Nature*. **493**, 97–100 (2013).
21. M. J. Roberts *et al.*, *J. Neurophysiol.* **93**, 2062–2072 (2005).
22. C. Y. Hsieh, S. J. Cruikshank, R. Metherate, *Brain Res.* **880**, 51–64 (2000).
23. C. Gratton *et al.*, *J. Neurosci.* **37**, 4405–4415 (2017).
24. K. A. Ferguson, J. A. Cardin, *Nat Rev Neurosci*. **21**, 80–92 (2020).
25. R. C. Froemke, *Annual Review of Neuroscience*. **38**, 195–219 (2015).
26. B. K. Murphy, K. D. Miller, *J. Neurosci.* **23**, 10040–10051 (2003).
27. X.-J. Wang, *Neuron*. **36**, 955–968 (2002).
28. N. H. Lam *et al.*, *bioRxiv* (2017), doi:http://dx.doi.org/10.1101/100347.
29. L. P. Sugrue, G. S. Corrado, W. T. Newsome, *Science*. **304**, 1782–1787 (2004).
30. M. A. Castro-Alamancos, T. Gulati, *J. Neurosci.* **34**, 12353–12367 (2014).
31. A. R. O. Martins, R. C. Froemke, *Nature Neuroscience*. **18**, 1483–1492 (2015).
32. R. C. Froemke, M. M. Merzenich, C. E. Schreiner, *Nature*. **450**, 425–429 (2007).
33. J. J. Letzkus *et al.*, *Nature*. **480**, 331–335 (2011).
34. A. F. T. Arnsten, C. D. Paspalas, N. J. Gamo, Y. Yang, M. Wang, *Trends Cogn. Sci. (Regul. Ed.)*. **14**, 365–375 (2010).
35. M. Usher, J. D. Cohen, D. Servan-Schreiber, J. Rajkowski, G. Aston-Jones, *Science*. **283**, 549–554 (1999).
36. J. D. Cohen, S. M. McClure, A. J. Yu, *Phil. Trans. R. Soc. B*. **362**, 933–942 (2007).
37. G. Aston-Jones, J. Rajkowski, J. Cohen, **46**, 1309–20 (1999).
38. G. A. Kane *et al.*, *Cogn Affect Behav Neurosci*. **17**, 1073–1083 (2017).
39. D. G. R. Tervo *et al.*, *Cell*. **159**, 21–32 (2014).
40. M. D. Fox, M. Greicius, *Front. Syst. Neurosci.* (2010), doi:10.3389/fnsys.2010.00019.

Acknowledgments: We thank Christian Büchel, Sander Nieuwenhuis, Wolf Singer and Alexander Thiele for discussion and comments on the manuscript and Klaus Wimmer for help with the implementation of the decision circuit; **Funding:** Alexander-von-Humboldt Foundation (postdoctoral fellowships to T.P. and R.v.d.B.); BMBF 161A130 (to A.K.E.); Catalan Agencia de Gestión de Ayudas Universitarias Programme 2017 SGR 1545 (to G.D.); Deutsche Forschungsgemeinschaft (DFG) DO1230/1 and DO1240/1 (to T.H.D.), SFB936/A3 (to A.K.E.), SFB936/A7 (to T.H.D.), SFB936/Z3 (to G.N. and T.H.D:); EU Horizon 2020 Research and Innovation Programme under Grant Agreements 720270 (HBP SGA1) and 785907 (HBP SGA2) (to G.D.); FLAG-ERA JTC (PCI2018-092891) (to A.P.-A.); International Brain Research Organization (to T.P.); Netherlands Organization for Scientific Research (NWO, dossiernummer 406-14-016, to T.H.D.); Spanish Research Project PSI2016-75688-P (Agencia Estatal de Investigación/Fondo Europeo de Desarrollo Regional, European Union) (to G.D.). **Author contributions:** T.P.: Conceptualization, Methodology, Formal Analysis, Investigation, Data Curation, Writing – Original Draft, Writing – Review & Editing, Visualization, Project Administration; A. P.-A.: Methodology, Formal Analysis, Writing – Review & Editing; T.M.: Formal Analysis, Investigation, Writing – Review & Editing; C. G.: Investigation, Writing – Review & Editing; R.L.v.d.B.: Conceptualization, Writing – Review & Editing; G.N.: Provided reagents, Writing – Review & Editing, K.T.: Methodology, Investigation, Writing – Review & Editing; A.K.E.: Resources, Writing – Review & Editing; G.D.: Methodology, Writing – Review & Editing, Supervision; T.H.D.: Conceptualization, Methodology, Writing – Original Draft, Writing – Review & Editing, Supervision; **Competing interests:** Authors declare no competing interests. **Data and materials availability:** All data and code needed in order to replicate the analyses, statistics and simulations shown in this article will be made available upon publication.

Supplementary Information

Materials and Methods

Pharmacological MEG experiment (resting-state and continuous perceptual choice task)

Participants

30 healthy human participants (16 females, age range 20-36, mean 26.7) participated in the study after informed consent. All included participants were non-smokers. The study was approved by the Ethics Committee of the Medical Association Hamburg. Two participants were excluded from analyses, one due to excessive MEG artifacts, the other due to not completing all 3 recording sessions. Thus, we report results from N=28 participants (15 females).

The present dataset was also used in a previous report (*18*), which focused on the effects of both drugs (see below) on the long-range temporal correlations in the local activity fluctuations. The present analyses of the correlations between these fluctuations across different cortical regions are independent from the results presented in this previous work. A different version of the behavioral result shown in Fig. 3A was also shown in the previous paper (*18*).

Experimental design

General protocol. We manipulated the levels of catecholamines (noradrenaline and dopamine) and acetylcholine through pharmacological intervention (Fig. 1A). Each participant completed three experimental sessions, consisting of drug or placebo intake at two time points, a waiting period of 3 hours, and an MEG recording session. During the recordings, participants were seated on a chair inside a magnetically shielded chamber. Each recording session consisted of six measurement blocks with different behavioral tasks (see below). Each block was 10 minutes long and followed by a short break of variable duration.

Pharmacological intervention. We tested for the effects of two different drugs in a double-blind, randomized, placebo-controlled, and cross-over experimental design. We used the selective noradrenaline transporter inhibitor atomoxetine to boost the levels of catecholamines (noradrenaline and dopamine (*13*, *14*)). We used the cholinesterase inhibitor donepezil to boost acetylcholine levels. A mannitol-aerosil mixture was administered as placebo. The dosages for both drugs were chosen to be below common clinical steady-state dosages and in accord with previous fMRI work showing clear effects of the same dosages on cortical processing (*15*, *41*): 40 mg for atomoxetine (clinical steady-state dose for adults: 80 mg) and 5 mg for donepezil (common clinical entry dose). All substances were encapsulated identically in order to render them visually indistinguishable. Peak plasma concentrations are reached ~3-4 hours after administration for donepezil (*42*) and 1-2 hours after administration for atomoxetine (*43*). In order to maximize plasma drug levels during MEG, participants received two pills in each session, 3 h and 1.5 h before MEG (Fig. 1A): placebo (t = -3 h) followed by atomoxetine (t = -1.5 h) in the ATOMOXETINE condition; donepezil (t = -3 h) followed by placebo (t = -1.5 h) in the DONEPEZIL condition; placebo at both times in the PLACEBO condition. The three sessions were scheduled at least 2 weeks apart to allow plasma levels to return to baseline (plasma half-life of atomoxetine: ~5.2 h – 21.6 h (*43*); half-life of donepezil: ~70 h).

Behavioral tasks. Within each session (and each of the above-defined pharmacological conditions), participants alternated between three different behavioral conditions, all entailing

absent or continuous sensory input (2 runs à 10 minutes per condition), here referred to as REST, TASK, and TASK-PRESSING (Fig. 1A, right; see also Supplementary Video 1). REST and TASK were steady-state conditions (absent or minimal variations in sensory input or motor output) tailored to quantifying *intrinsic* correlations between fluctuations in cortical activity. TASK-PRESSING was used to validate the behavioral results from the TASK condition. During REST, participants were instructed to fixate a green fixation disk (radius = 0.45º visual angle) in the center of an otherwise gray screen. During TASK and TASK-PRESSING, participants viewed a perceptually ambiguous 3D structure-from-motion stimulus, which was perceived as a rotating sphere (*44*). The stimulus subtended 21º of visual angle, consisted of 1000 dots (500 black and 500 white, radius: 0.18º of visual angle) arranged on a circular aperture presented on a mean-luminance gray background, and a green fixation dot in the center. In TASK, participants were instructed to count the number of changes in the perceived rotation direction and verbally report the total count at the end of the run. In TASK-PRESSING, the participants were instructed to press (and keep pressed) one of two buttons whenever they perceived a change in the rotation direction. The order of the conditions was as follows for 18 out of 28 participants: (1) REST, (2) TASK-PRESSING, (3) TASK, (4) REST, (5) TASK-PRESSING, (6) TASK. For 10 out of 28 participants the order was reversed: (1) TASK, (2) TASK-PRESSING, (3) REST, (4) TASK, (5) TASK-PRESSING, (6) REST.

The experiment was programmed in MATLAB (The MathWorks, Inc., Natick, United States), using the Psychophysics Toolbox extensions (*45*) (PTB-3).

Data acquisition. MEG was recorded using a whole-head CTF 275 MEG system (CTF Systems, Inc., Canada) at a sampling rate of 1200 Hz. In addition, eye movements and pupil diameter were recorded with an MEG-compatible EyeLink 1000 Long Range Mount system (SR Research, Osgoode, ON, Canada) and electrocardiogram (ECG) as well as vertical, horizontal and radial EOG was acquired using Ag/AgCl electrodes.

<u>Pupil and behavioral data analysis</u>

The pupil diameter recordings were preprocessed as follows: eye blinks as well as eye movements were identified using the manufacturer's default routines, then padded (+/- 200 ms), linearly interpolated and bandpass-filtered using a second-order Butterworth filter with a passband from 0.01 to 10 Hz. Next, the effect of blinks and saccades on pupil diameter was estimated through deconvolution and removed by means of linear regression (*46*). Mean pupil diameter was computed in a baseline interval from 6s to 3s prior to the start of each recording block and for all conditions (REST, TASK, TASK-PRESSING). Pupil signals were averaged across the two corresponding blocks. In some cases, pupil diameter was not recorded, or the signal was too noisy. If this was the case for both blocks of a session (placebo, atomoxetine or donepezil), the corresponding subject was not included in the respective analysis. The following number of subjects was excluded/included per combination of conditions: during REST-PLACEBO (N = 0/28), REST-ATOMOXETINE (N=0/28), REST-DONEPEZIL (N = 2/26), during TASK-PLACEBO (N = 0/28), TASK-ATOMOXETINE (N=0/28), TASK-DONEPEZIL (N = 1/27). Behavioral data from TASK and TASK-PRESSING was averaged across the two blocks, resulting in N=28 for all drug conditions for TASK. In the case of TASK-PRESSING, one participant had to be excluded due to missing triggers in the atomoxetine condition, resulting in N=27.

MEG signal processing

The MEG signal processing pipeline described is illustrated in Fig. S2A and entailed the following steps.

1) Preprocessing. The sensor-level MEG data were first preprocessed: strong transient muscle artifacts and squid jumps were detected through visual inspection as well as semi-automatic artifact rejection procedures, as implemented in the FieldTrip toolbox (*47*) for MATLAB. To this end, data segments contaminated by such artifacts (+/- 500 ms) were removed from the data (across all channels). Subsequently, the data were downsampled to 400 Hz split into low ([0.5-2]-40 Hz; the lower cutoff was variable across (but identical within) subjects at 0.5, 1 or 2 Hz) and high (>40 Hz) frequency components, using a 4th order Butterworth filter. Both signal components were separately submitted to independent component analysis (*48*) using the FastICA algorithm (*49*). Artifactual components (eye blinks/movements, muscle artifacts, heartbeat and other extra-cranial artifacts) were identified based on three established criteria (*50*): power spectrum, fluctuation in signal variance over time (in bins of 1s length), and topography. Artifact components were reconstructed and subtracted from the raw signal and low- and high frequencies were combined into a single data set. On average, 20 (+/- 14) artifact components were identified for the low-frequencies and 13 (+/- 7) artifactual components were identified for the high frequencies.

2) Spectral analysis. From the cleaned MEG signal, spectral estimates were obtained using Morlet's wavelets (*51*), similar to previous reports (*17*, *52*):

$$w(t,f) = \left(\sigma_t\sqrt{\pi}\right)^{-\frac{1}{2}} e^{-\frac{t^2}{2\sigma_t^2}}\, e^{-i2\pi f t} \qquad \text{(Eq. 1)}$$

We constructed wavelets for 17 logarithmically spaced (base 2) center frequencies, ranging from 4 Hz to 64 Hz. In keeping with previous work (*17*, *52*), the spectral band-width was set to half of an octave ($f/\sigma_t \sim 5.83$) and amplitude as well as phase estimates were obtained for consecutive, half-overlapping segments of a length of $\pm 3\sigma_t$. Segments that contained artifactual samples (see *Preprocessing*) were omitted from the analysis.

3) Source analysis. For the main analyses, we projected the sensor-level signal onto 400 vertices located on the cortical surface, resulting in an estimated source level signal $X_{src}(r,t,f)$. To this end, we estimated source-level power by means of adaptive spatial filtering (linear "beamforming") (*53*), separately for each participant and recording session. For each source location r and frequency f, a spatial filter $A(r,f)$ was computed according to:

$$A(r,f) = \left(L^T(r)C_{real}(f)^{-1}L(r)\right)^{-1} L^T(r)C(f)^{-1} \qquad \text{(Eq. 2)}$$

where L was the magnetic leadfield, T denoted matrix transpose, and $C_{real}(f)$ the real part of the (complex-valued and regularized) cross spectral density (CSD) matrix of the sensor-level data for frequency f. $A(r,f)$ contained three orthogonal projections. We used singular value decomposition of the CSD matrix to determine the direction of the dipole maximizing power (i.e. the first eigenvector) at location r. We then computed the corresponding spatial filter for this direction, henceforth referred to as $B(r,f)$. This filter was used to project the sensor-level data $X(t,f)$ onto that dominant dipole, as follows:

$$X_{src}(r,t,f) = B(r,f)X(t,f) \qquad \text{(Eq. 3)}$$

where $X_{src}(r,t,f)$ denoted the complex-valued, source-level spectral estimates for location r. Prior to computing the spatial filter, the CSD matrix was regularized with the mean of its diagonal multiplied by a scaling parameter α. For the results shown in the main section of this article, this parameter was chosen to be $\alpha = 0.3$ (see Fig. S6 for alternative values of α).

4) Orthogonalized power envelope correlations. Inter-regional correlations were computed as the correlations of the power estimates at carrier frequency f between two regions i and j, across all non-artifactual segments. In order to reduce spurious correlations arising from instantaneous signal leakage, we used a procedure established previously (*17*, *54*). Specifically, we orthogonalized each signal Y with respect to signal X according to:

$$Y_{\perp X}(t,f) = imag\ (Y(t,f)\ \frac{X(t,f)^*}{|X(t,f)|}) \qquad \text{(Eq. 4)}$$

where $Y_{\perp X}(t,f)$ was the signal $Y(t,f)$ orthogonalized with respect to signal $X(t,f)$ and * the complex conjugate. Next, the absolute value was taken and the resulting signal was squared, yielding source-level power envelopes, and log-transformed to render the distribution more normal. The orthogonalization was performed in two directions, $Y_{\perp X}(t,f)$ as well as $X_{\perp Y}(t,f)$. Correlation coefficients were computed for both directions and the resulting (Fisher transformed) values were averaged. Doing this for all pairs of vertices and for each frequency band resulted in a correlation matrix of size 400x400 for each of the 17 carrier frequencies. In what follows, we refer to these correlation matrices as 'functional connectivity (FC)' matrices.

In order to compare the empirical results to results obtained from simulations of a neural mass model (see: *Computational modeling* below), we repeated the above-described procedure for computing source-level FC matrices, but now at coarser granularity. To this end, we selected the 76 cortical regions of the Automatic Anatomical Labeling (AAL) atlas (*55*), excluding the cerebellum and subcortical regions (see Table S1 for included regions). Source locations were first arranged on an equally spaced grid (of 4 mm x 4 mm x 4 mm resolution) covering the entire brain and each grid point was either assigned to one of the 76 selected cortical AAL regions or omitted from further analysis. For each of the vertices that were assigned to one of the 76 AAL regions, frequency-specific source-level estimates for each time point $X_{src}(r,t,f)$ were computed following the procedure outlined above. Next, for each vertex within region i (with $i \in \{1,\ldots,76\}$, we computed its average correlation to all vertices of region j (after Fisher transformation). This was repeated for all vertices of region i after which the correlation values were again averaged across all vertices within region i. This procedure was repeated for all 76 regions, resulting in a 76x76 FC matrix for each of the 17 carrier frequencies.

Quantification of the topology of MEG correlation structure

Degree centrality. We computed frequency-resolved degree centrality $k(f)$ (i.e., collapsed across all nodes) as well as local degree $k_i(f)$ for each of the $i = 1 \ldots 400$ locations (Fig. S2B/C). Degree is defined by the number of edges that connect a given node to all other nodes in the network (*56*). To this end, the FC matrices of all subjects (400x400x28) were first submitted to a procedure described previously (*17*, *41*): for each connection between nodes i and j, where $i = 1 \ldots 400$ and $j = 1 \ldots 400$ we assessed if a connection was present as follows: a connection was determined to be present if the correlation between i and j was significantly larger ($P < 0.05$; two-sided t-test) than the correlations from i to all other nodes or from j to all other nodes. In case of a present connection, the corresponding entry in the adjacency matrix $A(i,j)$ was set to 1. If no

connection was present, $A(i,j)$ was set to 0. This was repeated for all possible pairs of vertices and the full adjacency matrix was computed. From this, we computed degree by:

$$D_i = (N-1)^{-1} \sum_{j=1}^{N} A(i,j) \qquad \text{(Eq. 5)}$$

where N denoted the number of cortical vertices (N = 400).

Statistical tests of MEG effects

Cortex-wide changes in cortical correlations. We adopted a previously described two-stage procedure for an unbiased statistical assessment of cortex-wide changes in power envelope correlations (*57*). The procedure is illustrated in Fig. S3. The rationale behind the analysis was as follows. Both neuromodulator classes (catecholamines and acetylcholine) might, in principle, increase correlations between some pairs of areas and, at the same time, suppress correlations between other pairs of areas (*58*). In this case, drug effects might cancel when averaging correlations indiscriminately across all area pairs and comparing average FC between conditions. Instead, our procedure first identified any pairs exhibiting drug-induced increases or decreases above a certain threshold and then tested if the fraction of these pairs was significantly different from what would be expected by chance, separately for pairs with increased and decreased correlations. This procedure was repeated across a wide range of frequencies, yielding the spectra of drug effects shown in Fig. 1E.

For each center frequency f, we statistically compared the Fisher-transformed FC matrices, across subjects, between the two drug conditions and placebo, using a two-sided paired t-test. Then we counted the number of significantly positively ($P < 0.05$ and $T > 0$) and the number of significantly negatively altered correlations ($P < 0.05$ and $T < 0$). The resulting value was divided by the number of possible connections M (with M = N*N-N, where N = 400 or N = 76, see above) to obtain the fraction of significantly altered correlations for both effect directions. This procedure was repeated for all 17 frequencies bands (Fig. S3). We employed a single threshold permutation procedure to derive P-values that accounted for multiple comparisons across frequencies (*59*). For each of N_p = 10000 permutations, the experimental labels (drug conditions) were randomly re-assigned within subjects and the aforementioned procedure was repeated. This resulted in a N_px17 matrix for both effect directions (significantly increased and significantly decreased correlations). Next, for each permutation, the maximum value across all frequencies (independently for increased and decreased correlations) was determined, yielding a maximum permutation distribution. In order to derive P-values, the empirical results were now compared to this maximum permutation distribution. This procedure is analogous to a single-threshold permutation test commonly applied in fMRI (*59*), with the single-threshold test being performed across frequencies instead of space (i.e., voxels). In order to test the robustness of the obtained results, we repeated the procedure described above using various alpha values for the initial paired t-test, ranging from a=0.01 to a=0.10, which led to numerically different, but qualitatively similar results (Fig. S7). Through applying an initial thresholding (t-test), spurious and weak changes in correlations are less likely to contribute to the observed result. The initial t-test thus ensures that only changes that are somewhat robust are taken into account.

Significant alterations in the correlations between two regions can be achieved in different ways. A decrease in correlations, for instance, can mean that a positive correlation becomes weaker, or that a negative correlation becomes more negative. However, only the former would qualify as a meaningful reduction in correlation, whereas the latter correlation gets numerically smaller (i.e., more negative), but stronger in terms of the linear dependence between two signals. Hence, a "significant decrease" does not always carry the same meaning, and the same is true for

increases. In this data set, the number of positive correlations by far outnumbered the number of negative correlations. In fact, in the alpha and beta frequency range, where the main effects for atomoxetine and donepezil are observed, more than 90% of all connections were positive (across all blocks, and contexts; placebo only). Thus, we interpret an increase (decrease) in correlation in terms of a positive correlation becoming stronger (weaker).

Cortex-wide changes in local cortical variability. Changes in the correlation between two signals can be driven by changes in their covariance (numerator of correlation coefficient) as well as changes in the variance of one or both of the signals (denominator). In order to rule out this possibility, we tested for drug-related changes in the variance of local power envelopes across frequencies (Fig. S5). To this end, we have adopted a procedure similar to the one employed to assess changes in cortex-wide activity correlations. First, we computed the variance of the power estimates across half-overlapping temporal segments (see *Spectral estimation*), separately for each of the 17 carrier frequencies. Next, we counted the fraction of nodes that exhibited significantly altered variance, separately for increases and decreases. We employed the same permutation procedure described above in order to derive corresponding permutation distributions from which P-values were computed (two-sided single threshold permutation test). Analogous to the 'fraction of significantly altered correlations', this procedure yielded, per frequency band, the fraction of vertices (nodes) with significantly positively or negatively altered variance.

Cortical circuit modeling

Large-scale neural mass model

Single node dynamics. We simulated neural population activity using a mean field model based on the Wilson-Cowan (WC) equations (*19*, *60*). Each local WC node consists of an excitatory and an inhibitory neuronal population (Fig. 2A). The dynamics of the E and I populations of each node are governed by the following stochastic differential equations:

$$\tau_E \frac{dE}{dt} = F_E(E,I) = -E + \sigma(w_{EE}E - w_{EI}I + b_E + \Delta b_E) + \eta, \qquad \text{(Eq. 6)}$$

$$\tau_I \frac{dI}{dt} = F_I(E,I) = -I + \sigma(w_{IE}E - w_{II}I + b_I + \Delta b_I) + \eta, \qquad \text{(Eq. 7)}$$

where E and I represent the firing rates of excitatory and inhibitory populations, respectively. Since we were interested in neural oscillations, the model parameters were chosen to generate oscillatory dynamics. The local synaptic weights interconnecting the excitatory and inhibitory populations were given as $w_{EE} = 12$, $w_{IE} = 16$, $w_{II} = 4$ and $w_{EI} = 12$. b_E and b_I represented external background inputs to the he excitatory and an inhibitory, respectively, $\Delta b_{E,I}$ represents task-induced input ($\Delta b_E = \Delta b_I = 0$, for resting dynamics), and η was uncorrelated Gaussian noise with amplitude equal to 0.005. Time constants of the were set to τ_E = 9 ms and τ_I = 18 ms. The (non-linear) transfer function converting input currents into output firing rates, $\sigma(u)$, was chosen to be a sigmoid:

$$\sigma(u) = \frac{1}{1+\exp(-gu)}, \qquad \text{(Eq. 8)}$$

where g determined the slope of the input-output function for both excitatory and inhibitory populations (i.e., response gain of the node).

The solutions (E^*, I^*), or fixed points, of the coupled equations 6 and 7, were given by $E^* = \sigma(w_{EE}E^* - w_{EI}I^* + b_E)$ and $I^* = \sigma(w_{IE}E^* - w_{II}I^* + b_I)$, yielding solutions depending on the external inputs (b_E, b_I), which are the bifurcation parameters of the system. In the (b_E, b_I)

parameter space, we observed a region of noise driven oscillations (i.e., a spiral; damped oscillations that, in the presence of noise, result in noisy oscillations) and a region of sustained oscillations (i.e., a limit cycle) (Fig. S8A).

Two coupled nodes. We first studied the effect of gain modulation on correlations during REST and TASK in a minimal network composed of two WC nodes (Fig. 2B, left). This step will provide intuitions before studying the whole-brain network composed of 76 nodes interconnected through a connectome. Let the excitatory populations of the nodes be connected through a reciprocal coupling c (in the two-node model, $c = 1$; see below for cortex-wide model) . The firing rates of node 1 evolve as:

$$\tau_E \frac{dE_1}{dt} = -E_1 + \sigma(w_{EE}E_1 - w_{EI}I_1 + cE_2 + b_E + \Delta b) + \eta, \qquad \text{(Eq. 9)}$$

$$\tau_I \frac{dI_1}{dt} = -r_I + \sigma(w_{IE}E_1 - w_{II}I_1 + b_I + \Delta b) + \eta, \qquad \text{(Eq. 10)}$$

and analogously for the firing rates, E_2 and I_2, of node 2.

To study the correlations between nodes in the parameter space, we used a linear noise approximation described in detail in the Supplementary Text. Using this approximation, we studied how changes in gain, i.e., $g \to g + \Delta g$, and inputs, i.e., $(b_E, b_I) \to (b_E + \Delta b, b_I + \Delta b)$, change the correlation between the two excitatory populations both during REST ($\Delta b = 0$) and TASK ($\Delta b \neq 0$). In this way, we can test hypotheses on the parameter changes induced by ATOMOXETINE and DONEPEZIL, assuming that TASK changed the background inputs b_E and b_I and the drugs changed g. Note that in the case of the two-node model the task-related change of the background inputs was equal for E and I, i.e., $\Delta b_E = \Delta b_I = \Delta b$.

In sum, the change in correlation between excitatory populations during REST was given as:

$$\Delta c_{EE} = c_{EE}(b_E, b_I, g + \Delta g) - c_{EE}(b_E, b_I, g), \qquad \text{(Eq. 11)}$$

and the change in correlation between excitatory populations during TASK was given as:

$$\Delta c_{EE} = c_{EE}(b_E + \Delta b, b_I + \Delta b, g + \Delta g) - c_{EE}(b_E + \Delta b, b_I + \Delta b, g), \qquad \text{(Eq. 12)}$$

Fig. 2C maps the change of correlations during REST under gain modulation in the (b_E, b_I)-plane. The combined effect of drugs on parameters b_E and b_I, and the effect of TASK, were obtained by translating the state of the system in this map.

Cortex-wide model. In order to directly compare the computational model to the empirical results, we simulated a cortex-wide variant of the model. For each of 76 cortical AAL nodes, the dynamics were governed by the following differential equations:

$$\tau_E \frac{dE_i}{dt} = -E_i + \sigma\left(w_{EE}E_i - w_{EI}I_i + c\sum_j C_{ij}E_j + b_E + \Delta b_E\right) + \eta, \qquad \text{(Eq. 13)}$$

$$\tau_I \frac{dI_i}{dt} = -r_i + \sigma(w_{IE}E_i - w_{II}I_i + b_I + \Delta b_I) + \eta, \qquad \text{(Eq. 14)}$$

where $i, j \in \{1,2,\dots,76\}$. In this cortex-wide model, an additional parameter was incorporated: long-range cortical connectivity between all possible pairs of regions, given by C_{ij}, which is scaled by the global coupling parameter c. The matrix C_{ij} was given by a structural connectivity matrix

used in previous studies (*61*, *62*) and was estimated by means of diffusion tensor imaging (DTI). Details can be found in the respective publications.

For the simulation, equations 13 and 14 were integrated using the Euler method with $\mathrm{dt} = 0.01$.

The model was run for a wide range of background inputs to excitatory (b_E) and inhibitory populations (b_I). In order to assess activity correlations (functional connectivity) in the model, we computed all-to-all (76x76) pairwise correlations between the raw time series of excitatory firing rates E_i. The model was simulated, for a total of 58.5s for each parameter combination prior to each run, initial conditions were randomized and the first 1.8 seconds were excluded from further analysis in order to avoid transient effects due to the initial conditions. All simulations and corresponding analyses were carried out in MATLAB2019b.

Identification of the oscillatory regime in the cortex-wide model. In all model-based analyses, we assume that the (healthy) human brain never resides in a dynamical regime of sustained oscillations (Fig. S8A, top panel; see also Supplemental Text). We therefore identified, and excluded, parameter combinations resulting in sustained oscillations in the cortex-wide model (see above). In order to identify parameter combinations where simulated population activity settled in the oscillatory regime, the cortex-wide model was simulated *without noise* (i.e., $\eta = 0$) for a total of 58.5s (plus 1.8s initialization, as outlined above). Next, for non-overlapping segments of 27 ms, the maximum and minimum of r_E was computed. In a regime of noise-driven (damped) oscillations, the activity relaxed back to a fixed point over time (Fig. S8A, middle and bottom). Hence, the computed maximum and the minimum should converge on the same value, whereas in a regime of sustained oscillations, the maximum and the minimum will remain different throughout the entire simulation (Fig. S8A, top). Consequently, the regime was defined as non-oscillatory or *noise driven*, if: (1) the maximum and minimum were identical at any point in time or (2) the difference between maximum and minimum decreased monotonously over time (indicative of a damped oscillation); if none of the two were true, the signal was defined as a sustained oscillation (see Supplementary Text).

Model fitting procedure. We fit the free parameters of the cortex-wide model through an iterative procedure. The purpose of this procedure was to identify two working points, mimicking the two behavioral conditions (REST and TASK). First, we estimated the global coupling parameter α. This this end, we simulated the cortex-wide model (76 regions) over a range of 41 different coupling parameters α (with $\alpha \in \{0, 0.05, \dots, 2\}$) and across 61x61 combinations of background inputs (with $I_E \in \{-4, -3.9, \dots, -1\}$ and $I_I \in \{-5, -4.9, \dots, -2\}$). We then estimated the similarity of the simulated functional connectivity matrix FC_{sim} and the empirical functional connectivity matrix FC_{emp} (Rest and Placebo only; averaged across frequencies that showed significant changes for both drugs; see Fig 1E), separately for each combination of I_E and I_I, by means of a distance metric δ based on Pearson correlation (*63*):

$$\delta = 1 - \left(\frac{1}{N} \sum_{i=1}^{N} \rho^{FC_{sim}, FC_{i,emp}} - \left(\left\langle \frac{1}{N} \sum_{i=1}^{N} FC_{i,emp} \right\rangle - \langle FC_{sim} \rangle \right)^2 \right) \qquad \text{(Eq. 15)}$$

where $\rho^{FC_{sim}, FC_{i,emp}}$ was the correlation (i.e., pattern similarity) between the empirical FC matrix for subject i (averaged across frequencies, with $i \in \{1, 2, \dots, 28\}$) and the simulated FC matrix and $\langle\ \rangle$ denotes the average across all possible connections. We averaged the resulting distance values δ across all external background inputs (b_E and b_I), while omitting parameter combinations where the network activity settled into a regime of sustained oscillations (see above).

This resulted in a mean distance $\langle\delta\rangle$ for each level of global coupling α (Fig. S8C). Additionally, we repeated the procedure but instead computed Pearson correlation between FC_{sim} and FC_{emp} (Fig. S8D). We identified the level of α where the mean distance $\langle\delta\rangle$ between FC_{sim} and FC_{emp} was minimized ($\alpha = 1.2$). The parameter with lowest $\langle\delta\rangle$ also yields a high correlation between FC_{sim} and FC_{emp} (Fig. S8D).

After having fixed the global coupling parameter, we aimed to identify the combination of b_E and b_I for each individual participant, that resulted in the highest similarity between FC_{sim} and FC_{emp} during REST and PLACEBO (i.e., lowest distance). To this end, we first identified the combinations of b_E and b_I where the distance between FC_{sim} and FC_{emp} was below the 2.5th percentile. The resulting binary matrix was then submitted to a clustering procedure (using SPM's 'bwlabel' function) and the single largest cluster was extracted. This was to reduce the influence of spurious correlations on the fitting procedure. Next, the geometric center of the largest cluster was computed and defined as the best fitting combination of I_E and I_I, yielding a working point for $REST_{sim}$. This procedure was repeated separately for each of the 28 participants (Fig. S8F). In order to determine the corresponding TASK parameter $TASK_{sim}$, we assumed that the constant visual stimulation during TASK increases both excitatory (b_E) and inhibitory drive (b_I), consistent with electrophysiological recordings in rodent visual cortex V1 (*20*, *64*) (see Supplementary Text). Thus, in order to simulate TASK ($TASK_{sim}$) we increased the background input to both excitatory and inhibitory populations, i.e., b_E and b_I. We chose to increase background input to inhibitory populations by $\Delta b_I = 0.475$ and to excitatory population by $\Delta b_E = 0.25$ (Fig. 2D,E, cortex-wide model). Note that, for simplicity, we here assume that the change in background inputs due to TASK is global and homogenous across all nodes and identical for all participants. This assumption is certainly oversimplified and model fits can likely be improved by heterogeneous scaling of these effects (*65*) as well as by taking individual differences into account.

Local microcircuit models

Microcircuit model of local node. In order to assess how changes in neural gain can be achieved through specific changes in synaptic weights, we simulated a model of a canonical cortical microcircuit, as a conductance-based neural network (Fig. 2F) comprised of 400 leaky integrate-and-fire units (20% inhibitory). Model equations and parameters follow (*27*), with some modifications as mentioned below. The model architecture is depicted in Fig. 2F. The membrane potential dynamics of the excitatory units below threshold were governed by:

$$C_m \frac{dV(t)}{dt} = g_L(V(t) - V_L) - I_{syn}(t)\ ) \qquad \text{(Eq. 16)}$$

Here, $I_{syn}(t)$ denotes the total synaptic current, which was composed of two glutamatergic excitatory currents (with AMPA and NMDA components) and GABAergic inhibitory currents. External input as well as external noise to the network were mediated exclusively via AMPA receptors. Baseline parameters were identical to (*27*) with the exception of $g_{IE,GABA} = 1.99$ (weight of inhibitory to excitatory synapses) and $g_{ext,AMPA} = 2.5$ (weight of external input on excitatory neurons). Moreover, the rate of the external Poisson input to excitatory and inhibitory neurons was changed to $v_{ext} = 881\ Hz$ (originally $v_{ext} = 2400\ Hz$). From these baseline values, we parametrically scaled the conductance parameters $g_{EE,AMPA}$ and $g_{IE,GABA}$ (AMPA-mediated recurrent excitation and feedback inhibition, respectively) in order to achieve plausible spontaneous dynamics (see Supplemental Text and Fig. S10 for details). Next, we presented the network with stimuli in form of external excitatory input (added to the background input) to all

excitatory cells, mediated through AMPA receptors, and assessed the effect on resulting excitatory population firing rate (*26*). In visual cortex, neurons respond to stimuli with increasing contrast with higher firing rates. This relation between a neurons output and the visual input strength is well-described by a hyperbolic ratio function known as the Naka-Rushton function:

$$R(C) = R_{max}\frac{C^n}{C^n + C_{50}^n} + S \qquad \text{(Eq. 17)}$$

where $R(C)$ is the firing rate at input contrast C, R_{max} is the response gain, S reflects the level of the spontaneous (background) activity and C_{50} is the stimulus strength that yields a firing rate at half the maximum. Using this equation, we generated a set of stimuli (with varying "contrast", i.e., varying levels of C) that were transformed into firing rates of different frequency and were subsequently fed into the network as an AMPA-mediated excitatory Poisson input. The parameters used in the current study were identical to the parameters used in a previous theoretical study on the effects of excitation and inhibition on response gain of single neurons (*26*): $R_{max} = 2000\ Hz$, $C = 20.133$, $n = 1.2$ and $S = 0$. This approach allowed us to measure the response of a neural population to inputs of varying contrast strength, which is typically depicted as a contrast-response curve (Fig. 2F, bottom panel). In order to assess the effect of excitation-inhibition ratio on the shape of the contrast-response curve, we either decreased or increased feedback inhibition in the model, through adjusting $g_{EI,GABA}$ (see Supplemental Text for details). Using nonlinear least squares estimation, we fit the hyperbolic ratio function (Eq. 17), with four free parameters (R_{max}, C_{50}^n, S and n), to the resulting contrast-response curves. This yielded, among others, response gain parameters (R_{max}) for different levels of feedback inhibition (Fig. 2F, bottom panel). The network was simulated for 3s per parameter combination, with a similar period of external stimulation. All simulations and analyses were carried out in Python 2.7.15, using the Brian spiking neural network simulator (version 1.4.4) (*66*, *67*), the Elephant toolbox for Python as well as custom code. The Python code for the model simulations was adapted from publicly available code (*68*).

Decision circuit. In order to understand how the increase in reported perceptual transitions during ambiguous visual stimulation under atomoxetine (Fig. 3A) could be related to changes in synaptic activity, we extended the above neural circuit by equipping the model with two excitatory populations, which competed for dominance via common feedback inhibition. The synaptic equations were identical to the homogeneous microcircuit described in the previous section. Unless stated otherwise, model architecture and parameters were identical to the original description (*27*) (Fig. 3B, left). The circuit consisted of N=2000 leaky integrate-and-fire neurons, endowed with full connectivity. 1600 of the neurons were excitatory and 400 inhibitory. The excitatory cells were assigned to one of three subpopulations: two decision populations (240 neurons each), D1 and D2, as well as one non-specific population (DN; 1120 neurons). The two decision populations were assumed to represent the populations that encode the two possible perceived rotation directions of the ambiguous stimulus. All neurons, excitatory and inhibitory, of all populations (D1, D2, DN and I) received independent AMPA-mediated excitatory background input in the form of a Poisson spike train with a frequency of 2880 Hz. In addition, the neurons of the decision populations D1 and D2 received independent AMPA-mediated excitatory input with a mean firing rate of 55.6 Hz which was to reflect the stimulus-related sensory input. The identical mean in input to both decision populations was to mimic the ambiguous nature of the structure-from-motion stimulus. Recurrent connections within D1 and D2 were stronger than connections within DN, by a factor of $w_+ = 1.6$. The network was simulated for 600s and population firing rates were estimated for time bins of 100 ms length. Perceptual transitions in the model were defined as the time points where the firing rate of one decision population exceeded the firing rate of the other decision

population, i.e., at those time points where the difference between firing rates of D1 and D2 changed in sign (Fig. S11). In order to attenuate the effect of very fast fluctuations on the number of perceptual transitions, we low-pass filtered the firing rates of both decision populations prior to computing the perceptual transitions (cutoff frequency 1 Hz). In order to understand the effect of execution and inhibition on perceptual transitions, we again modified feedback inhibition by means of adjusting $g_{EI,GABA}$ and computing the number of perceptual transitions for each level of feedback inhibition. For each level of feedback inhibition, the network was simulated 20 times.

Pharmacological behavioral experiment (value-based choice task)

Participants

We measured 32 participants (21 females, age range 20 – 36, mean 27.28) that performed two sessions of a value-based choice task (Fig. S13A) after informed consent. All included participants were non-smokers. The study was approved by the Ethical Committee responsible for the University Medical Center Hamburg-Eppendorf. We excluded three participants from the analysis based on foraging efficiency, which we here defined as the fraction of collected rewards over the total number of available rewards: we excluded participants whose foraging efficiency deviated more than three times the median from the median, scaled by a constant (c≈1.4826, using MATLAB's 'isoutlier' function). Based on this criterion, the same three participants were excluded for both experimental sessions (Fig. S13D). This resulted in in 29 included participants.

Experimental design

General protocol. We manipulated the levels of catecholamines (noradrenaline and dopamine) in a double-blind, randomized, placebo-controlled pharmacological intervention using atomoxetine (see above, section *Pharmacological MEG experiment*). Each participant completed two experimental sessions, consisting of drug or placebo intake, a waiting period of 1.5 h, and performance of the behavioral task during MEG recordings. During task performance, participants were seated on a chair inside a magnetically shielded chamber and the (visual) task stimuli were presented on a screen in front of them (Fig. S13A). Because this was a standard trial-based task design entailing many sensory and motor transients, the MEG data from this task were not used for the analysis of correlations between intrinsic fluctuations in cortical activity. The MEG data will be reported in a separate study.

Behavioral task. We used a modified version of a dynamic foraging used in a previous monkey physiology study (*29*). Participants chose freely between two visual target stimuli (identified by orientation, randomized by position), which were associated with different histories of monetary rewards. The sequence of events during each trial is shown in Fig. S13A. Participants were asked to fixate a white box in the center of a uniform grey background. Each trial started with the presentation of the two targets (full-contrast Gabor patches with vertical or horizontal orientations) that were presented on either side of the fixation mark (eccentricity ~8.5°, diameter ~4.25° visual angle). The horizontal target's (left vs. right) location was randomly drawn on each trial, under the constraint that it would appear equally frequently on each side within a block of trials with equal 'income ratio' (see below). After a 0. 5-1.5 s delay, the fixation mark changed shape (from box to diamond), prompting the subject's choice. Participants then pressed a button with their left or right index finger to choose the target at the corresponding location. After another variable delay (2-5 s), subjects received auditory feedback on the outcome of their choice (reward or no reward) by means of a low- or high-pitched tone (low: 200 Hz, high: 880 Hz; each with duration: 150 ms). The mapping of the tones to 'reward' or 'no-reward' was counterbalanced across participants and

instructed before the start of each experimental session. If the participant had not yet responded within a deadline of 3 s, another tone (440 Hz, 50 ms) signaled their missed response (no reward), and the trial was aborted. Targets disappeared after feedback tone, so that only the fixation mark remained for an inter-trial-interval (ITIS) 2-5 s, during which the subjects kept fixating. The next trial started upon the new onset of the targets. Trial duration varied between 4.5 and 11.5 s plus reaction time (reaction times could range between 0 and 3 s) respectively, with an average trial duration of 8 s plus reaction time (0 to 3s). Participants completed 525 trials in each experimental session, taking about 75 min, excluding breaks in between blocks of 100 trials.

Each target was baited with a separate Poisson process for generating rewards, under the following constraints (Fig. S13A, B): (i) the 'income' (i.e., reward) rate averaged across both targets was 0.8 rewards per trial; (ii) the ratios between the reward rates associated with each target for a given block of trials (see below) were drawn from a predefined set {7:1, 5:1, 3:1, 1:1, 1:1, 1:3, 1:5, 1:7}; (iii) a reward assigned to a target (i.e., orientation) remained available there until this target was chosen; (iv) when a reward was available at a target, no new reward could become available there (i.e., there was never more than one reward available per target). Correspondingly, both or one or none of the targets could carry a reward in a given trial – the rewards associated with both targets were uncoupled.

The ratios between reward rates ('local income ratios' (*29*)) changed between blocks of trials, without this being signaled to the participants. The block duration was sampled from a uniform distribution which ranged between 40 and 60 trials (Fig. 13B). Subjects were not informed about these changes. Because of this dynamic nature of the foraging task, a successful policy is to integrate rewards earned from choosing each target, but only 'locally' in time, over the last trials (see (*29*) and *Behavioral modeling*).

Subjects were not instructed about the statistics of the process generating the rewards. They were only instructed to (i) try to earn as many rewards as possible and that this would translate to a bonus payment at the end of the session; and (ii) to be 'flexible' in their behavior because the relative income of the two targets could change over time.

Subjects were rewarded €0-20 bonus based on performance. The lower boundary was chance level performance; the maximum bonus could be earned by performing on par with an ideal observer model, which chose based on full information about the reward ratio at every trial.

Pupil analysis

The pupil diameter recordings were preprocessed similar to experiment 1 (see *Pharmacological MEG experiment*): eye blinks as well as eye movements were identified using the manufacturer's default routines, then padded (+/- 200 ms), linearly interpolated and bandpass-filtered using a second-order Butterworth filter with a passband from 0.01 to 10 Hz. Next, the effect of blinks and saccades on pupil diameter was estimated through deconvolution and removed by means of linear regression (*46*). Mean pupil diameter was computed in a pre-target baseline interval from 500 ms to 0 ms prior to target onset. Pupil recordings were not available for 4 participants. Hence, the analysis was performed for the remaining 25.

Behavioral modelling

We fitted an algorithmic model of behavior to quantify the effects of atomoxetine on the different computations governing decision-making in the task. Our model extended the model previously developed to account for monkey choices in the task (*29*, *69*). A schematic of the model is depicted in Fig. 3E. In words, model choices were computed through the following steps: (i) leaky integration of the rewards gathered from choosing each option over the recent trials (locally in time); (ii) combination of the 'incomes' earned from each reward into a relative value signal, the

'local factional income' (LFI); (iii) non-linear (*softmax*) transformation of LFI into a probability of choosing the horizontal option; (iv) a weighted contribution of a win-stay-loose-switch (WSLS) heuristic and (v) a weighted contribution of general bias (preference for one of the targets) to the final choice probability. Leaky reward integration was applied in order to account for rapid adaption to the hidden changes in income ratio across blocks (see above: *Experimental design* and (*29*, *69*)).

Please note that the WSLS heuristic had been suppressed, by design, in the monkey study (*29*) through a so-called 'change-over-delay' (i.e., punishment for switching targets after one choice). We did not include this change-over-delay in our task to render the foraging task even more naturalistic. We found that subjects' behavior could be well accounted for by a linear mixture of the leaky reward integration described by steps (i)-(iii), the heuristic from step (iv) (Fig. S13E).

In line with (*29*), we fitted the model by minimizing the negative log-likelihood between the model choice probability from step (iv) and the subjects' binary choices, giving the set of parameter values (for similar approach see (*29*)). We first found the minimum in a rough grid search. These parameter values were then used as starting point for MATLAB's 'fminsearchbnd'.

For each trial *t*, the model computed LI_{hor}, the 'local income' earned from choosing the horizontal option, as follows:

$$LI_{hor} = \frac{1}{e^{-t/\tau}} \cdot o_{1:t}^{hor}, \qquad \text{(Eq. 18)}$$

where $o_{1:t}^{hor}$ were the outcomes of horizontal choices on trials $1{:}\,t$ and τ was the reward integration time constant (model leak $\lambda = \frac{1}{\tau}$). Rewards earned from choosing the horizontal option were coded as 1 and all non-rewarded horizontal choices, or choices to the vertical option (irrespective of reward) were coded as 0. The same equation was used to update LI_{ver}, now coding rewards earned from choosing the vertical option as 1 and all other outcomes as 0.

The local fractional income LFI_{hor} was defined as:

$$LFI_{hor} = \frac{LI_{hor}}{\sum(LI_{hor}, LI_{ver})}, \qquad \text{(Eq. 19)}$$

LFI_{hor} was transformed into the choice probability $p(c_t = hor)$, defined with respect to the horizontal target, through a sigmoidal (softmax) function (*69*):

$$p(c = hor) = \frac{e^{\beta \cdot LFI_{hor}}}{e^{\beta \cdot LFI_{hor}} + e^{\beta \cdot LFI_{ver}}}, \qquad \text{(Eq. 20)}$$

where β was the 'inverse temperature' parameter" that governed decision noise, i.e. corrupting the mapping from LFI to the behavioral choice. β ranged from 0 (no noise) to infinity.

Choice probability $p(c_t = hor)$ was further transformed by linear combination with the simple switching (WSLS) mechanism defined as follows:

$$WSLS(c_t | o_{t-1}) = \begin{cases} o_{t-1} \neq 0, \; c_t = c_{t-1} \\ o_{t-1} = 0, \; c_t = -1 * c_{t-1} \end{cases}, \qquad \text{(Eq. 21)}$$

Note that decision noise (1/β) only affected the integration of reward over trials, not WSLS. This was because we assumed (and confirmed through formal model comparison, Fig. S13F) that internal noise corrupted the reward integration more than the simple WSLS heuristic.

Finally, $p(c_t = hor)$ was transformed into the final choice probability estimate by linear combination with general bias δ, which could range between -1 (all choices to vertical option) to 1 (all choices to horizontal option.

In sum, the dynamics of choice probability (model quantity fitted to the data), was given by:

$$p(c_t = hor | \, c_{1:t-1}, o_{1:t-1}) = \left(1 - \delta\left((1 - \omega_{WSLS}) \cdot \left(\frac{e^{\beta \cdot LFI_{hor}}}{e^{\beta \cdot LFI_{hor}} + e^{\beta \cdot LFI_{ver}}}\right) \omega_{WSLS} \cdot WSLS\right) + \delta\right)$$

(Eq. 22),

where $p(c_t = hor|\, c_{1:t-1}, o_{1:t-1})$ was the probability of horizontal choice on trial *t*, given the choices made and outcomes (rewards) received from trial 1 to trial *t-1*, ω_{WSLS} was a free parameter (ranging from 0 to 1) that controlled the contribution of the WSLS heuristic to choice probability.

In the results reported here, the model included all 4 free parameters for each of the participants. However, we see in the data that the level of bias and tendency to rely on the WSLS heuristic varies substantially between participants. In a separate version of the analysis, where we determined the best-fitting set of parameters per participant using cross-validation, we replicate the increase of the softmax parameter under influence of atomoxetine (data not shown).

Supplementary Text

Assumptions for large-scale (Wilson Cowan) modeling

Our large-scale modeling approach was based on two assumptions. In the following, we discuss the physiological evidence supporting these assumptions.

Assumption 1. Cortex operates in a regime of noise driven, not sustained, oscillations. We assumed that the cerebral cortex generally operates in a regime of noise-driven oscillations, rather than self-sustained oscillations (Fig. 2C; Fig. S8A). In the noise-driven (also referred to as fluctuation-driven) regime, stochastic fluctuations in activity drive dampened oscillations in the local nodes. Superposition of such dampened oscillations, triggered at random moments in time, give rise to the same ongoing variations in the amplitude of band-limited activity that are commonly observed in electrophysiological data under steady-state conditions (*17*, *70*), including the current data set (*18*). The time-varying amplitudes (power envelopes) were used to compute the inter-regional correlations in the MEG data (Fig. S2). Consequently, we eliminated all parameter combinations that fell outside of this regime of noise-driven oscillations from further consideration (see Materials and Method, for identification of the parameters producing sustained oscillations to be excluded).

Assumption 2. TASK increased the drive of both, E- and I-populations. We assumed that the change from REST to TASK corresponded to a shift of the model's dynamical regime in an upward-rightward direction in the $(\boldsymbol{b_E}, \boldsymbol{b_I})$-plane (Fig. 2C, area defined by dashed outline). This means that background input to both excitatory and inhibitory neural populations is increased for all nodes of the model. This assumption rests on the straightforward notion that our elementary visual task increased the input to sensory and task-related cortical regions. There is substantial evidence for the idea that cortical circuits generally operate in a regime of rough balance between excitation and inhibition (*71*, *72*). Specifically, sensory input increases not only feedforward excitation (i.e., feedforward drive of pyramidal cells), but also feedforward inhibition (i.e., feedforward drive of interneurons) in sensory cortex (*73*, *74*), and it is assumed that this motif repeats across the cortical hierarchy (*71*) likely augmented through circuit motifs for feedback inhibition (*75*). Correspondingly, we assumed that the visual task increased the background input to excitatory and inhibitory populations in a (loosely) balanced fashion, with a slight dominance of feedforward inhibition in the case of the cortex-wide model (see Fig. 2D,E). Indeed, recent evidence from rodent physiology shows that visual stimulation leads to a more pronounced inhibitory response (*20*, *64*) compared to the excitatory response, consistent with sensory input leading to even stronger feedforward inhibition compared to feedforward excitation. Note that this was in line with *Assumption 1*: if the task-induced increase in excitation was much larger than the task-induced increase in inhibition, the dynamical regime of the network would change to

oscillatory, inconsistent with physiological evidence.

Hypotheses for large-scale (Wilson-Cowan) modeling

In this section, we review the physiological evidence, from which we derived our hypotheses pertaining to the impact of catecholamines and acetylcholine on cortical population dynamics.

Hypothesis 1. Catecholamines and acetylcholine increase the gain of the input/output function of cortical neurons and cortical populations. The notion that catecholamines (NA, DA) increase the gain of input/output functions has long been established at the single-neuron level (*1*, *7*, *76*). More recent evidence points to an increase in E/I (disinhibition) through a long-lasting suppression of ongoing inhibitory inputs to pyramidal cells under noradrenaline (*9*, *31*), which can produce substantial gain increase at the single-cell level (Fig. 2F). This, in turn, should translate into gain modulation at the level of the cortical mass activity described by the Wilson-Cowan model. The same hypothesis has been tested in other modeling studies into the catecholaminergic modulation of cortical mass activity (*58*, *77*).

Physiological evidence indicates that acetylcholine also increases gain at the single-neuron level (*8*, *78–80*). However, cholinergic effects on the excitatory and inhibitory influences on pyramidal cells that determine their gain seem to be confined to the suppression of stimulus-evoked, phasic inhibitory inputs and their longer-lasting, plastic effects affect primarily stimulus-responsive neurons (*25*, *32*). Hence, if the cholinergic E/I and gain modulation affects a smaller fraction of neurons in the local population for a shorter durations, then it should translate into a smaller impact on the net gain of the entire cortical area (node) described by the Wilson-Cowan model. This is also consistent with the idea that the cholinergic system is less diffusely organized as traditionally assumed (*81*, *82*), and with mounting evidence demonstrating direct synaptic cholinergic connections (wired transmission) as opposed to the spatially more coarse impact of volume transmission (*81*).

Hypothesis 2. Acetylcholine and/or catecholamines decrease intra-cortical coupling. Substantial evidence suggests that acetylcholine in particular suppresses intra-cortical signaling (*22*), for example reducing spatial integration through lateral interactions in primary visual cortex (*15*, *21*) and perception (*23*). This is consistent with computational accounts assuming that acetylcholine reduces the impact of prior beliefs relative external evidence in inference (*10*). While our neural mass model does not differentiate between feedforward, lateral, and feedback long-range connections, the majority of intra-cortical long-range connections are lateral and feedback (*83*). Thus, a reduction of intra-cortical interactions can be translated into a reduction of the global coupling parameter in our mass model. While similar changes of global coupling may, in principle, hold for catecholamines, our model simulations showed that the catecholamine effect could be explained solely with an increase in gain (Fig. 2) – a change in global coupling was only required for explaining the acetylcholine effect.

Dynamics of a single-node Wilson Cowan model

The mass dynamics of the local nodes were governed by the control parameters and $\boldsymbol{I_E}$ and $\boldsymbol{I_I}$, representing external drive to the excitatory and inhibitory populations, respectively. The parameters of the model were tuned such that the model is in a dynamical state close to a so-called supercritical Adronov-Hopf bifurcation. The 'Hopf-bifurcation' separates a regime in which the system relaxes to a stable fixed point, or *focus*, by drawing a spiral in the phase space (noise-driven, damped oscillations; Fig. 2C; Fig. S8A, middle and bottom), and a regime in which the network activity settles into a *limit-cycle*, a closed orbit in the phase space corresponding to a

periodic solution (sustained oscillations; Fig. 2C and Fig. S8A, top). When the system settles into the focus, intrinsic noise induces stochastic oscillations and gives rise to a broad spectral density with a single peak. In contrast, in the limit-cycle, autonomous regular oscillations are observed, with a spectral density presenting a narrow peak (Fig. S8E). The parameters $\boldsymbol{w}$ as well as $\boldsymbol{I_E}$ and $\boldsymbol{I_I}$ were loosely adjusted in order to produce dynamics in the vicinity of a supercritical Hopf bifurcation. In the context of the Hopf-bifurcation, the term 'supercritical' is not to be confused with the same term referring to the power law scaling behavior (*84*, *85*).

<u>Linear noise approximation for two-nodes Wilson Cowan model</u>

We used a linear noise approximation to study the linear fluctuations around the system's fixed points, i.e., $E_i = E_i^* + \delta E_i$ and $I_i = I_i^* + \delta I_i$, where the fixed points are given by:

$$E_i^* = \sigma\left(w_{EE}E_i^* - w_{EI}I_i^* + cE_j^* + b_E + \Delta b\right), \quad (23)$$

$$I_i^* = \sigma(w_{IE}E_i^* - w_{II}I_i^* + b_I + \Delta b). \quad (24)$$

Dynamic equations for the linear fluctuations can be written as:

$$\frac{d}{dt}\delta\boldsymbol{r} = \boldsymbol{A}\delta\boldsymbol{r} + \boldsymbol{\eta}, \quad (25)$$

where $\delta\boldsymbol{r} = [\delta E_1, \delta I_1, \delta E_2, \delta I_2]$, $\boldsymbol{\eta}$ is the noise matrix, and $\boldsymbol{A}$ is the Jacobian matrix of the system evaluated at the fixed points, given by the 4-by-4 matrix:

$$A_{\alpha\beta} = \left[\frac{1}{\tau_\alpha}\frac{\partial F_\alpha}{\partial \beta}\right]_{(E_1^*, I_1^*, E_2^*, I_2^*)}, \quad (26)$$

where $\alpha, \beta \in \{E_1, I_1, E_2, I_2\}$. Noting that $\sigma'(u) = g\sigma(u)[1 - \sigma(u)]$ and that, by symmetry, $E_1^* = E_2^* = E^*$ and $I_1^* = I_2^* = I^*$, we get:

$$A = \begin{bmatrix} A_{EE} & A_{EI} & K & 0 \\ A_{IE} & A_{II} & 0 & 0 \\ K & 0 & A_{EE} & A_{EI} \\ 0 & 0 & A_{IE} & A_{II} \end{bmatrix}, \quad (27)$$

where:

$$\tau_E A_{EE} = -1 + w_{EE}gE^*(1 - E^*), \quad (28)$$
$$\tau_E A_{EI} = -w_{EI}gE^*(1 - E^*), \quad (29)$$
$$\tau_E K = cgE^*(1 - E^*), \quad (30)$$
$$\tau_I A_{IE} = w_{IE}gI^*(1 - I^*), \quad (31)$$
$$\tau_I A_{II} = -1 - w_{II}gI^*(1 - I^*), \quad (32)$$

The stationary covariances $\boldsymbol{C_v} = \langle\delta\boldsymbol{r}\delta\boldsymbol{r^T}\rangle$ between all populations can be obtained through the Jacobian matrix, by solving the following equation:

$$\boldsymbol{AC_v} + \boldsymbol{C_v A^T} + \boldsymbol{Q_n} = 0, \qquad (33)$$

where $\boldsymbol{Q_n} = \langle \boldsymbol{\eta\eta^T} \rangle$ is the covariance matrix of the noise (which is diagonal for uncorrelated white noise) and the superscript T denotes the transpose operator. Note that the Jacobian matrix depends on the system's fixed points, i.e., it depends on the state of the nonlinear system and, thus, on the external inputs (b_E, b_I). Hence, the correlations are also a function of the parameters (b_E, b_I). Equation 20 can be solved using the eigen-decomposition of the Jacobian matrix evaluated at the fixed points: $A = LDL^{-1}$, where D is a diagonal matrix containing the eigenvalues of A, denoted λ_i, and the columns of matrix L are the eigenvectors of A. Multiplying Equation 20 by L^{-1} from the left and by $L^{-\dagger}$ from the right (the superscript dagger being the conjugate transpose) we get:

$$\boldsymbol{C_v} = \boldsymbol{LML^{\dagger}}, \qquad (34)$$

where $\boldsymbol{M}$ is given by: $M_{ij} = -\tilde{Q}_{ij}/(\lambda_i + \lambda_j^*)$, and $\boldsymbol{\tilde{Q}} = \boldsymbol{L^{-1}ML^{-\dagger}}$.

Simulation and fitting of cortex-wide Wilson Cowan model

Identification of dynamical regime. The dynamical regime was defined as noise- or fluctuation-driven if: (1) the maximum and minimum were identical at any point in time or (2) the difference between maximum and minimum decreased monotonously over time (indicative of a damped oscillation). If none of the two were true, the signal was defined as a sustained oscillation. Note that this approach does not allow to distinguish between the two regimes with full certainty as the time scale with which the amplitude of an oscillation decays back to the fixed point increases as one approaches the Hopf-bifurcation from the fluctuation-driven regime (see Fig. S8A, middle and bottom panels). Thus, the closer the dynamical regime is to the Hopf-bifurcation, the more simulation time is required to accurately distinguish a sustained oscillation from a damped oscillation.

Microcircuit modeling (spiking neurons)

Microcircuit model of local node. We simulated the leaky integrate-and-fire circuit across a range of parameters to identify a stable working point where the network exhibits dynamics reminiscent of the "asynchronous state" (*86*). We defined the asynchronous state as being characterized by a low spontaneous firing rate (1-5 Hz) and low mean pairwise spike correlations (r < 0.1; averaged across all pairs of excitatory units). In addition, we identified a working point in the "synchronized state", where the pairwise spike correlations where relatively high (r > 0.3), but spontaneous firing rates were comparable to the asynchronous state. This was achieved by changing AMPA-mediated recurrent excitation as well as the GABA-mediated feedback inhibition in a multiplicative manner: we started from the baseline parameters of (*27*), with some minor changes (see Materials and Methods), and multiplied $g_{EE,AMPA}$ (i.e., conductance of recurrent AMPA receptors) and $g_{IE,GABA}$ (i.e., conductance of GABAergic feedback inhibition) with 24 and 12 (respectively) linearly spaced values, ranging from 0.2 to 5 and 2.7 to 5. Fig. S10A shows spike rate (left) and mean pairwise spike correlations (right) for all parameter combinations. While for the main part of the analysis, we focus on the asynchronous state (shown in Fig. 2F; mean firing rate FR = 4.14 Hz; mean pairwise spike correlations r = 0.05), we further wanted to test whether the observed effect of feedback inhibition on response gain holds true also for the synchronous state. To this end, we first identified a dynamical regime reminiscent of the synchronous state, with low firing rates (FR = 5.11 Hz) but relatively high pairwise spike correlations (r = 0.27). We

find that, irrespective of state, a reduction in feedback inhibition leads to an increase in response gain (Fig. S10B).

Tuning of parameters of decision circuit model. This model was based on a circuit model of decision-making developed to explain neural dynamics and choice behavior in standard two-alternative forced choice tasks, entailing trials of a few seconds of duration (*27*). Without further adjustments to the parameters of the decision circuit, the network dynamics would rapidly enter one of the two possible attractor states, reflecting the preference for decision 1 or decision 2 (Fig. S11A). Moreover, without sufficient levels of external drive or noise, the network would dwell in those states indefinitely, as the lateral inhibition would dominate over the external input or the magnitude of the noise. In order to introduce dynamics that exceed beyond short timescales (single trials), we increased the level of background noise as well as the strength of the external stimulus. This way, we identified a state where the model would switch continuously between two attractors. Once this point was identified, we only changed feedback inhibition in order to assess the influence of E/I ratio on perceptual transitions (Fig. 3B, right).

Note that other studies that employed neural circuit models similar to the one used here for the study of perceptual fluctuations during ambiguous stimulations (*87*) also included adaptation as an alternative mechanistic explanation for perceptual transitions. For the sake of simplicity, we did not consider this in the current circuit.

Previous results on catecholaminergic stimulation on behavioral exploration

We found that elevating catecholamine levels via noradrenaline increases behavioral exploration during both perceptual and value-guided choice tasks (Fig. 3). This result confirms a key prediction from an influential account of the role of the locus coeruleus noradrenaline system in the regulation of the tradeoff between behavioral exploration and exploitation (*1*). In this view, high tonic noradrenaline levels boost behavioral variability. While this is detrimental to performance in many tasks (e.g. perceptual decision-making in the absence of evidence volatility), increased variability can boost performance in tasks entailing hidden environmental changes, as our foraging task, by promoting the exploration of alternative behaviors (in the case of our task: choosing the other target) (*1*, *35*, *36*).

This idea was developed from the observation that monkey choice behavior was more variable during periods of high tonic firing of the locus coeruleus (*35*, *37*). These early studies entailed simple perceptual choice tasks without hidden environmental changes, so that behavioral variability could only impair performance. More recent work in rodents has linked tonic locus coeruleus activity to increased behavioral variability in value-based choice in changing environments (*38*, *39*). In particular, Kane et al. (2014) found an increase of decision noise under chemogenetic stimulation of locus coeruleus tonic activity during a foraging task (*38*), in line with our current results in humans.

One pharmacological study in humans used a protocol similar to ours (40 mg of atomoxetine vs. placebo, however administered 3 rather than 1.5 h before experiment) during a gambling task (*88*). The authors decomposed different modes of behavioral exploration (random vs. directed) and found a *decrease* in random exploration under atomoxetine (*88*). This finding appears to be at odds with the above animal work as well as the increase in behavioral variability reported in the two tasks (bistable perception and dynamic foraging) of the present study. Two possible differences between studies may account for this apparent discrepancy. First, the predominant effect of atomoxetine on tonic versus phasic noradrenaline levels may have differed between the studies. Such differences in atomoxetine effects may have occurred due to the different latencies of the behavioral measurements relative to drug intake in both studies (1.5 vs. 3 h), due to inter-session differences in baseline arousal/noradrenaline levels, and/or due to inter-

individual differences in atomoxetine sensitivity between participants. In the present study, we found a robust increase of baseline pupil diameter under atomoxetine, an effect consistent with increased tonic noradrenaline levels (*89–91*). This effect was not tested in (*88*). The decreased choice variability in this study may have resulted from a predominant increase in phasic noradrenaline release, a possibility in line with (*1*) and also alluded to by the authors (*88*). Another possibility is that the different findings are due to differential contributions of dopamine and noradrenaline. Atomoxetine also increases dopamine levels in prefrontal cortex (*14*), which, in turn, has also been linked to behavioral exploration (*92*).

Comparison with previous neuroimaging studies of catecholamine effects on intrinsic activity correlations

It is instructive to compare our results with those of previous pharmacological neuroimaging studies that have investigated the effects of catecholamines and acetylcholine on correlations of intrinsic fluctuations of cortical population signals (for see detailed review see (*93*)). A PET study found a behavioral context-dependence of catecholamine effects reminiscent of the one reported in our current study: under clonidine (an α2-adrenergic auto-receptor agonist that reduces locus coeruleus activity), cortical and cortico-thalamic coupling *increased* during a cognitive task but *decreased* during rest (*94*).

An fMRI study using a similar pharmacological protocol as ours (40 mg of atomoxetine vs. placebo; drug administration ~1.5 h prior to start of the fMRI session) found an overall decrease in intrinsic correlations during rest (*41*). Here, we found no effect of atomoxetine on intrinsic correlations during rest. This may reflect differences in the underlying neurophysiological signals (fMRI vs. of band-limited MEG power), or genuine, state-dependent differences of the neuromodulator effects on cortical networks.

Our modeling results (Fig. 2) demonstrate how subtle differences in the location on the (b_E, b_I)-plane can lead to qualitatively different effects (i.e., sign reversals) of changes in catecholamine-mediated increases in gain on intrinsic correlations in activity. It is conceivable that systematic differences in environmental factors (e.g. scanner noise or experimental setup), participants' age, or in their baseline arousal levels affect the location on the (b_E, b_I)-plane. These subtle differences in location could potentially explain effects of different sign, despite the administration of the same drug with identical dosage.

Supplementary references

41. R. L. van den Brink *et al.*, *The Journal of Neuroscience*. **36**, 7865–7876 (2016).
42. Tiseo, Rogers, Friedhoff, *British Journal of Clinical Pharmacology*. **46**, 13–18 (1998).
43. J.-M. Sauer, B. J. Ring, J. W. Witcher, *Clin Pharmacokinet*. **44**, 571–590 (2005).
44. H. Wallach, D. N. O'connell, *J Exp Psychol*. **45**, 205–217 (1953).
45. D. H. Brainard, *Spat Vis*. **10**, 433–436 (1997).
46. T. Knapen *et al.*, *PLoS ONE*. **11**, e0155574 (2016).
47. R. Oostenveld, P. Fries, E. Maris, J.-M. Schoffelen, *Comput Intell Neurosci*. **2011**, 156869 (2011).
48. A. J. Bell, T. J. Sejnowski, *Neural Comput*. **7**, 1129–1159 (1995).
49. A. Hyvarinen, *IEEE Transactions on Neural Networks*. **10**, 626–634 (1999).
50. J. F. Hipp, M. Siegel, *Frontiers in Human Neuroscience*. **7** (2013), doi:10.3389/fnhum.2013.00338.
51. null Tallon-Baudry, null Bertrand, *Trends Cogn. Sci. (Regul. Ed.)*. **3**, 151–162 (1999).
52. M. Siems, A. Pape, J. Hipp, M. Siegel, *NeuroImage* (2016), doi:10.1016/j.neuroimage.2016.01.055.
53. V. B. Veen, W. van Drongelen, M. Yuchtman, A. Suzuki, *Biomedical ….* **44**, 867–80 (1997).
54. M. J. Brookes, M. W. Woolrich, G. R. Barnes, *NeuroImage*. **63**, 910–920 (2012).
55. N. Tzourio-Mazoyer *et al.*, *NeuroImage*. **15**, 273–289 (2002).
56. M. Rubinov, O. Sporns, *Neuroimage*. **52**, 1059–1069 (2010).
57. D. J. Hawellek *et al.*, *Journal of Neuroscience*. **33**, 17072–17080 (2013).
58. E. Eldar, J. D. Cohen, Y. Niv, **16**, 1146–53 (2013).
59. T. E. Nichols, A. P. Holmes, *Human Brain Mapping*. **15**, 1–25 (2002).
60. G. Deco, V. Jirsa, A. R. McIntosh, O. Sporns, R. Kotter, *Proceedings of the National Academy of Sciences*. **106**, 10302–10307 (2009).

61. G. Deco, M. L. Kringelbach, V. K. Jirsa, P. Ritter, *Sci Rep*. **7**, 3095 (2017).
62. G. Deco *et al.*, *Current Biology*. **28**, 3065-3074.e6 (2018).
63. M. Demirtaş *et al.*, *Neuron*. **101**, 1181-1194.e13 (2019).
64. H. Adesnik, *Neuron*. **95**, 1147-1159.e4 (2017).
65. M. Demirtaş *et al.*, *Neuron*. **101**, 1181-1194.e13 (2019).
66. D. F. M. Goodman, *Frontiers in Neuroscience*. **3**, 192–197 (2009).
67. D. F. Goodman, M. Stimberg, P. Yger, R. Brette, *BMC Neuroscience*. **15**, P199 (2014).
68. K. Wimmer *et al.*, *Nature Communications*. **6** (2015), doi:10.1038/ncomms7177.
69. G. S. Corrado, L. P. Sugrue, H. Sebastian Seung, W. T. Newsome, *Journal of the Experimental Analysis of Behavior*. **84**, 581–617 (2005).
70. D. A. Leopold, Y. Murayama, N. K. Logothetis, *Cereb. Cortex*. **13**, 422–433 (2003).
71. M. N. Shadlen, W. T. Newsome, *J. Neurosci.* **18**, 3870–3896 (1998).
72. C. van Vreeswijk, H. Sompolinsky, *Science*. **274**, 1724–1726 (1996).
73. J. S. McCasland, L. S. Hibbard, *J. Neurosci.* **17**, 5509–5527 (1997).
74. H. A. Swadlow, *Philos. Trans. R. Soc. Lond., B, Biol. Sci.* **357**, 1717–1727 (2002).
75. T. Womelsdorf, T. A. Valiante, N. T. Sahin, K. J. Miller, P. Tiesinga, *Nat Neurosci*. **17**, 1031–1039 (2014).
76. L. M. Hurley, D. M. Devilbiss, B. D. Waterhouse, *Curr. Opin. Neurobiol.* **14**, 488–495 (2004).
77. J. M. Shine, M. J. Aburn, M. Breakspear, R. A. Poldrack, *eLife*. **7** (2018), doi:10.7554/eLife.31130.
78. J. L. Herrero, M. A. Gieselmann, A. Thiele, *Front. Neural Circuits*. **11**, 106 (2017).
79. S. Soma, S. Shimegi, H. Osaki, H. Sato, *J. Neurophysiol.* **107**, 283–291 (2012).
80. A. A. Disney, C. Aoki, M. J. Hawken, *Neuron*. **56**, 701–713 (2007).
81. M. Sarter, V. Parikh, W. M. Howe, *Nature Reviews Neuroscience*. **10**, 383–390 (2009).
82. B. Hangya, S. P. Ranade, M. Lorenc, A. Kepecs, *Cell*. **162**, 1155–1168 (2015).
83. D. J. Felleman, D. C. Van Essen, *Cereb. Cortex*. **1**, 1–47 (1991).
84. J. M. Beggs, D. Plenz, *J. Neurosci.* **23**, 11167–11177 (2003).
85. S.-S. Poil, R. Hardstone, H. D. Mansvelder, K. Linkenkaer-Hansen, *Journal of Neuroscience*. **32**, 9817–9823 (2012).
86. A. Renart *et al.*, **327**, 587–590 (2010).
87. R. Moreno-Bote, J. Rinzel, N. Rubin, *J. Neurophysiol.* **98**, 1125–1139 (2007).
88. C. M. Warren *et al.*, *PLoS ONE*. **12**, e0176034 (2017).
89. M. J. McGinley, S. V. David, D. A. McCormick, *Neuron*. **87**, 179–192 (2015).
90. S. Joshi, Y. Li, R. M. Kalwani, J. I. Gold, *Neuron*. **89**, 221–234 (2016).
91. J. Reimer *et al.*, *Nature Communications*. **7**, 13289 (2016).
92. M. J. Frank, B. B. Doll, J. Oas-Terpstra, F. Moreno, *Nature Neuroscience*. **12**, 1062–1068 (2009).
93. R. L. van den Brink, T. Pfeffer, T. H. Donner, *Front. Hum. Neurosci.* **13**, 340 (2019).
94. J. T. Coull, C. Büchel, K. J. Friston, C. D. Frith, *NeuroImage*. **10**, 705–715 (1999).

Supplementary Figures

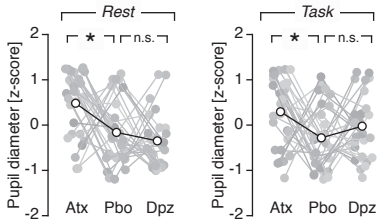

Fig. S1. Drug effect on baseline pupil diameter.
Baseline pupil diameter after the administration of atomoxetine (Atx), placebo (Pbo) or donepezil (Dpz), separately for rest (left) and task (right). (*) indicates $P < 0.05$ (paired t-test).

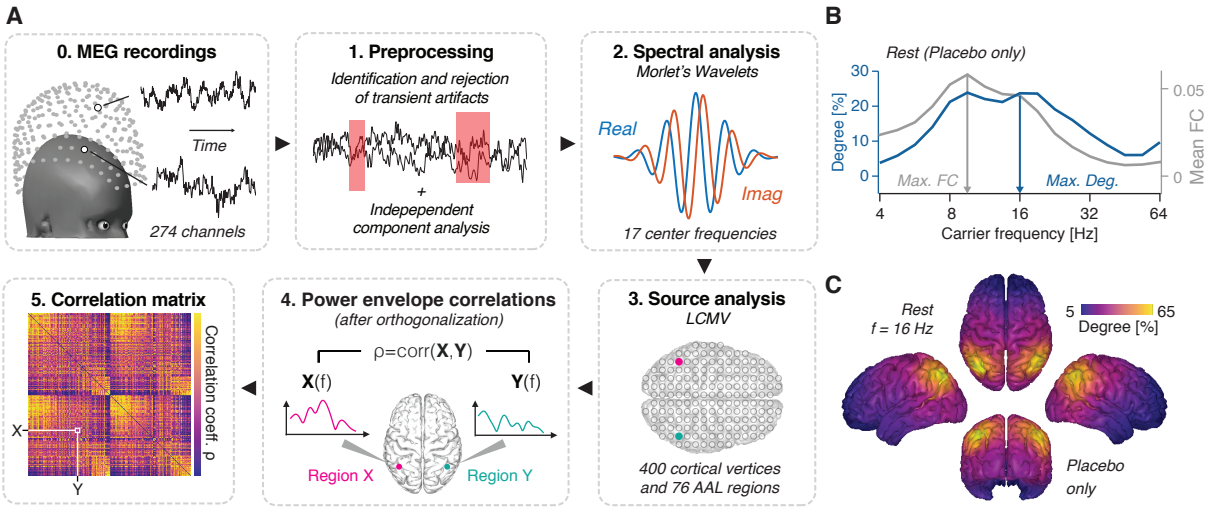

Fig. S2. Quantifying cortex-wide correlation structure.
(A) (0.) Whole-head magnetoencephalography (MEG) was recorded using 274 recording channels located in a helmet above the participants head**.** (1.) The sensor-level signal was cleaned from transient and sustained artifacts (e.g. muscle and heart beat artifacts, respectively). (2.) Spectral estimates were obtained from the cleaned sensor-level signal using complex wavelet convolution. (3.) From the spectral estimates and individual head models, source level power time series were obtained, (4.) from which orthogonalized power envelope correlations were computed. (5.) This resulted in functional connectivity (FC) matrices for each of the 17 carrier frequency bands of interest. **(B)** Global degree (Materials and Methods) and mean FC as a function of frequency during the rest-placebo condition. **(C)** Spatial map of degree during the rest-placebo condition**.** Correlations peak in the 'alpha' (center frequency 9.51 Hz; B) and 'beta' frequency range (center frequency 16 Hz; B), with strongest 'connectedness' (degree) in left and right posterior parietal cortex. These results are consistent with previous reports using an analogous approach to resting-state MEG data (*17*).

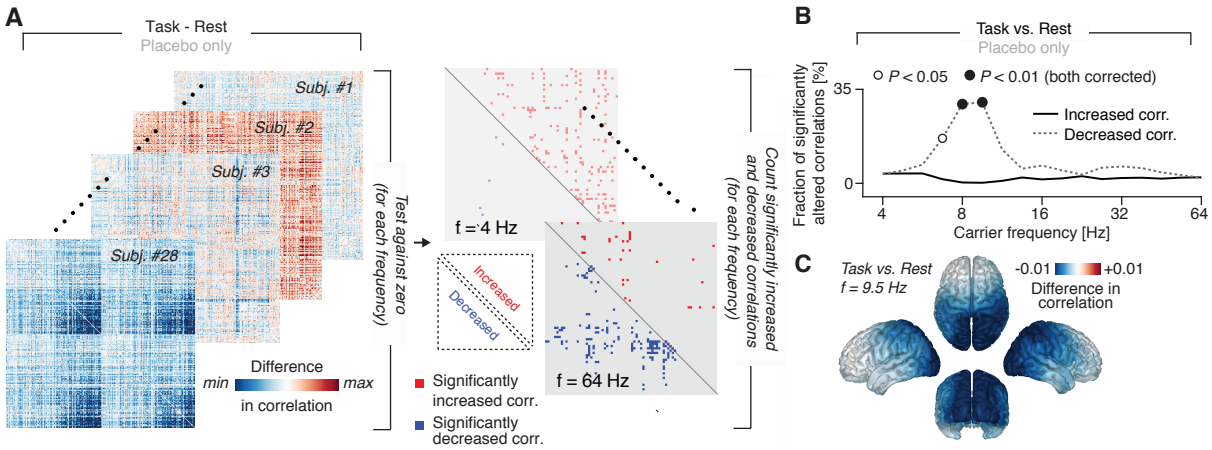

Fig. S3. Quantifying task effects on cortical activity correlations.
(A) Illustration of the approach to quantify changes in the global activity correlation structure: First, the difference between two conditions (here: rest and task; placebo only) was tested by means of a paired t-test. Next, the number of statistically significantly (P < 0.05; uncorrected) increased (in red) and significantly decreased (in blue) connections was counted. **(B)** A fraction of significantly altered correlations (negative and positive alterations) can be computed for each frequency band of interest, resulting in a spectrum of fraction of significantly altered correlations. **(C)** Spatial distribution of the difference in correlation between task and rest (placebo only) at a carrier frequency of 9.5 Hz.

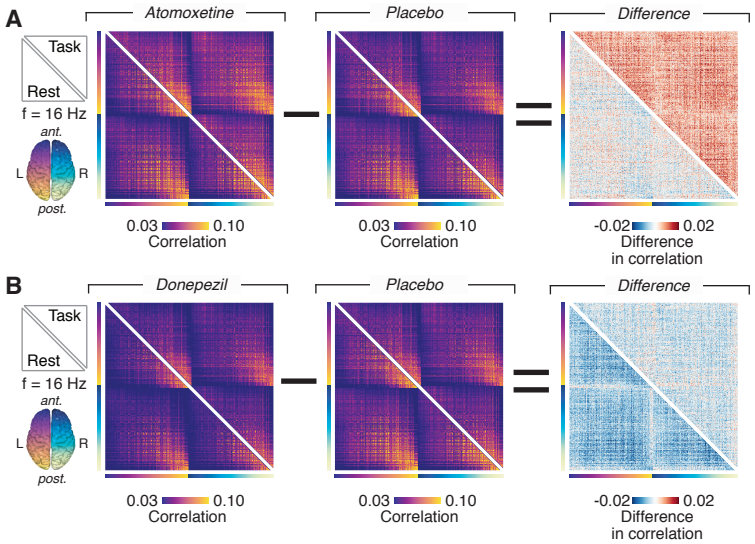

Fig. S4. Quantifying drug effects on cortical activity correlations.
(A) Functional connectivity matrices (only lower or upper triangular parts; at a carrier frequency of 16 Hz) for atomoxetine, placebo and the difference between the two (lower triangular part: during rest; upper triangular part: during task) and **(B)** for donepezil, placebo and the difference between the two.

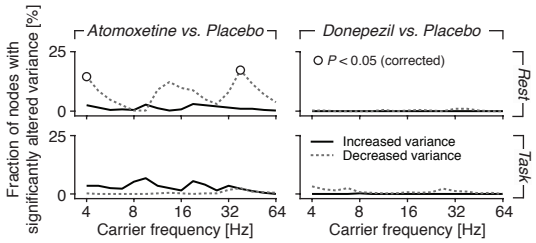

Fig. S5. Changes in correlations were not driven by changes in local variance.
Atomoxetine (left) induced a weak increase in the fraction of nodes with reduced power envelope variance compared to placebo during rest (open circles indicate $P < 0.05$, corrected for multiple comparisons across frequencies). Atomoxetine produced a tendency towards the opposite effect during task (increase in local variance) during task, albeit not statistically significant. Donepezil (right) did not lead to any significant alterations in local power envelope variance. The pattern of local variance changes under atomoxetine (decrease during rest, increase during task) cannot explain the observed pattern of changes in correlations under atomoxetine (no effect during rest, increase during task). In particular, an increase in local variance during task would reduce, not increase, correlations, because the local variance enters in the denominator in the computation of the correlation coefficient.

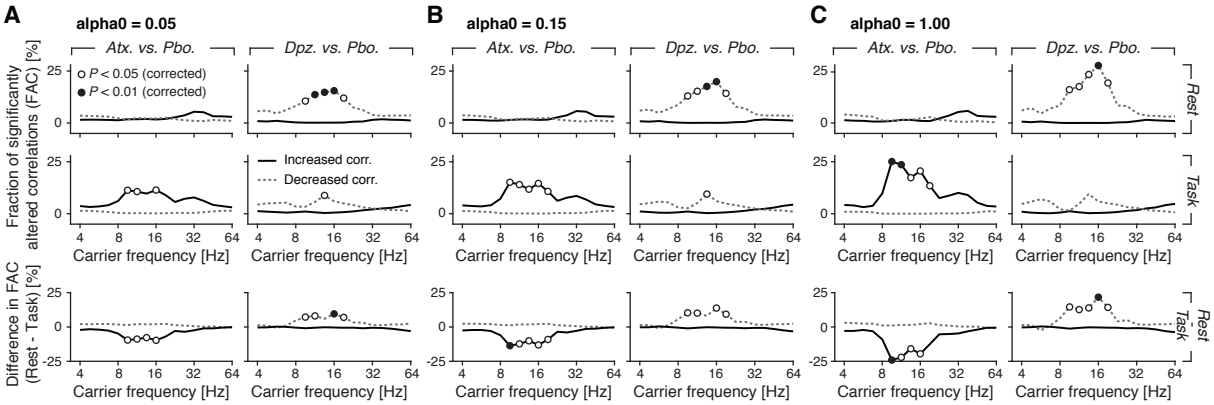

Fig. S6. Fraction of significantly altered correlations for various regularization parameters.
(A-C) Fraction of significantly altered correlations (FAC; as in Fig. 1E) for different regularization parameters used for the source reconstruction procedure (see Materials and Methods; panel A: $\alpha = 0.05$; panel B: $\alpha = 0.15$; panel C: $\alpha = 1.00$). In the top row, the drug effects during rest are shown, in the middle row the effects during task (Left: Atomoxetine vs. placebo; Right: donepezil vs. placebo). The bottom row shows the effect of behavioral state (or context), i.e., the difference between the drug effect during Rest and the drug effect during Task. Significant differences are indicated by open circles ($P < 0.05$) and filled circles ($P < 0.01$; two-sided single-threshold permutation test).

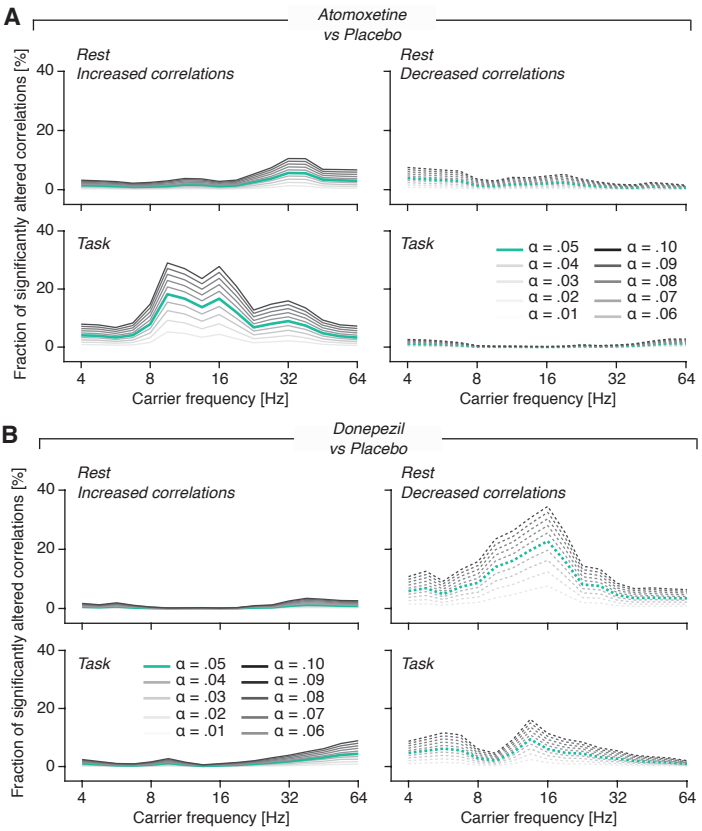

Fig. S7. Fraction of significantly altered correlations for various alpha-thresholds parameters.
The choice of the alpha-level for the initial paired t-test (Fig. 1E) does not affect the general qualitative pattern of the drug-induced changes in the fraction of significantly altered correlations. **(A)** Fraction of altered correlations as in Fig. 1E, but for various different alpha-values (for the initial t-test; see Materials and Methods), ranging from 0.01 to 0.10, for atomoxetine and **(B)** donepezil.

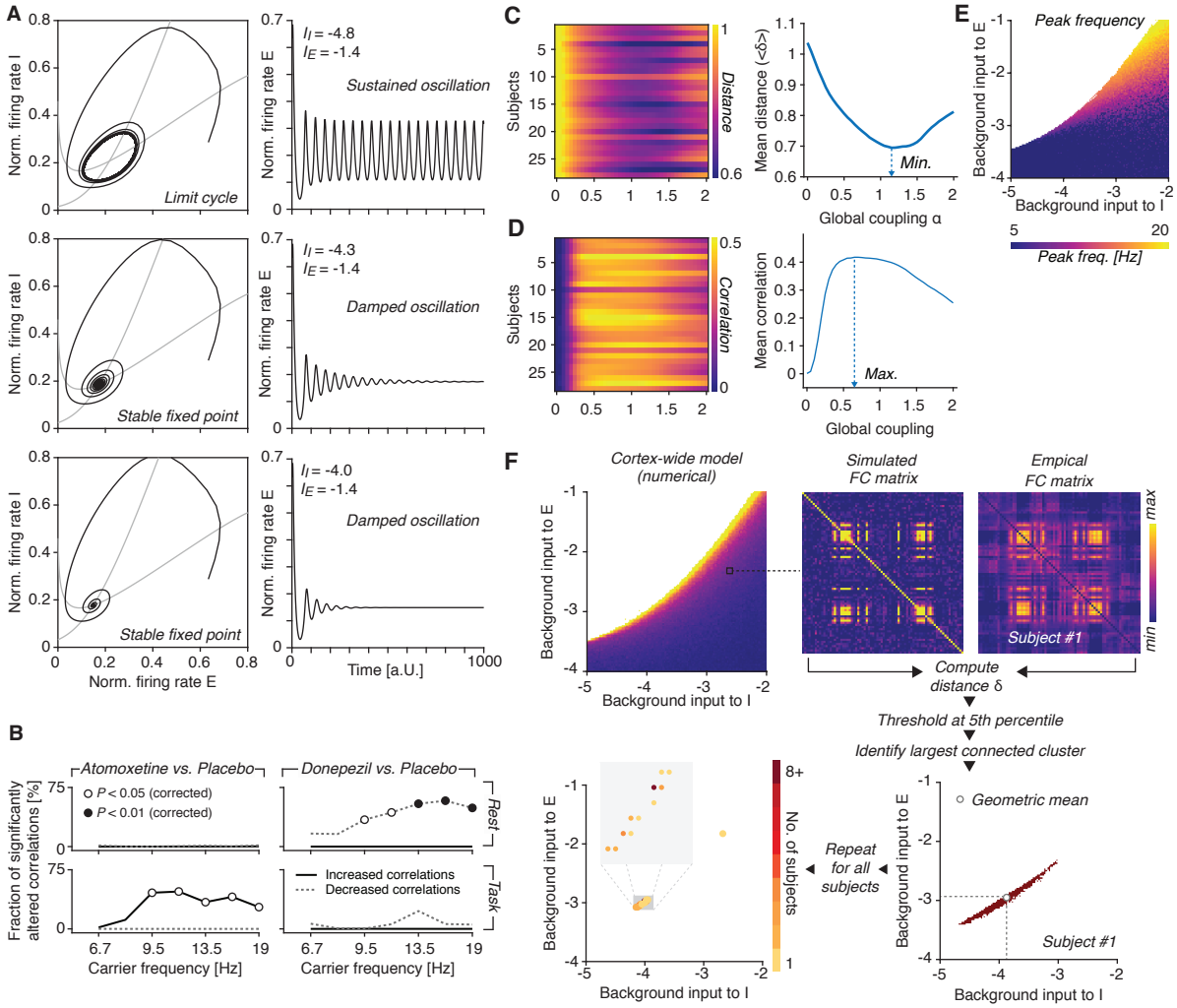

Fig. S8. Dynamics of the Wilson-Cowan models and fitting procedure of the cortex-wide model.
(A) Dynamics of a single Wilson-Cowan node around the Hopf-bifurcation. Top: Dynamics in the oscillatory regime, exhibiting sustained oscillations. Middle and bottom: Dynamics in the noise-driven regime, exhibiting damped oscillations. **(B)** The drug effects on fraction of significantly altered correlations for 76 AAL nodes and selected carrier frequency bands (ranging from ~6.7 to ~19 Hz). **(C)** Estimation of the global coupling parameter. Left: across all participants and a number of background input parameters (to E and I), the similarity (here: distance; see Materials and Methods) between the simulated and the empirical functional connectivity matrices was computed. Right: Distance (averaged across participants) for various levels of global coupling. **(D)** Same as (C), but for Pearson correlation. **(E)** Peak frequency of the model for various levels of background inputs to E and I. **(F)** Illustration of the fitting procedure: for each combination of background inputs to E and I, as well as every participant, the distance between simulated and empirical FC (rest and placebo only) was computed. The resulting distance matrix was thresholded at the 2.5th percentile (all values larger were set to zero, all others to 1) and the largest connected cluster was identified. The geometric mean of this cluster was defined as the best-fitting value for a given participant. Repeating this procedure for all participants resulted in 28 fitted resting state parameters.

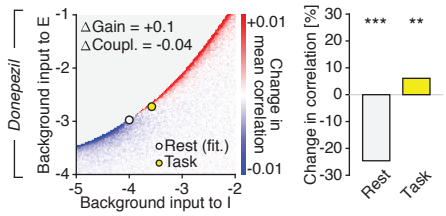

Fig. S9. Effect of identical gain increase as in Fig. 2D (+0.1) combined with decrease of global coupling (-0.04) in cortex-wide model. This produces a similar decrease of cortex-wide correlations during rest as observed in the data under donepezil, but an increase in correlations during task, different from both, the donepezil and atomoxetine data. Note that the specific pattern of these effect depends on the amplitude of the task-related shift in the $(\boldsymbol{b_E}, \boldsymbol{b_I})$-plane; the parameter changes used here may capture the observed donepezil effect with a different task-related shift in the $(\boldsymbol{b_E}, \boldsymbol{b_I})$-plane. However, an equally big gain increase under acetylcholine as under catecholamines seems unlikely, given existing physiological data (Supplementary Text) and given the difference between the effects of both drugs on the number of perceptual transitions during the task (Fig. 3A).

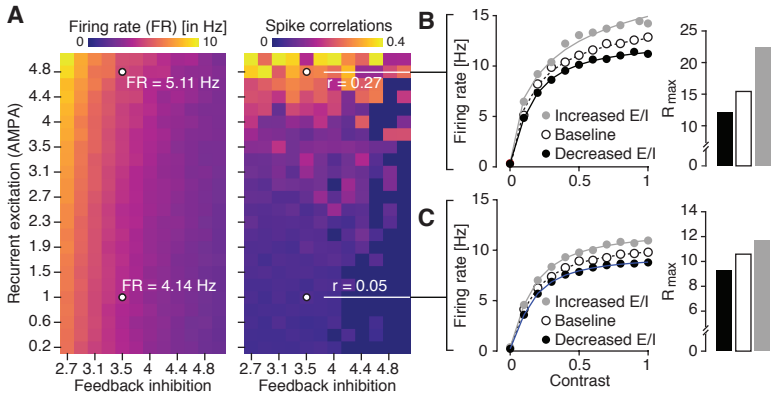

Fig. S10. Increased E/I ratio increases response gain in asynchronous and synchronous states.
(A) The parameters of the leaky integrate-and-fire model were tuned such that the network dynamics are indicative of a synchronized state (depicted pairwise spike count correlations r = 0.27) and low baseline firing rate (depicted FR = 5.11 Hz) or an asynchronous regime (pairwise spike count correlations r = 0.05), with comparable baseline firing rate (FR = 4.14 Hz). **(B)** The effects of altered feedback inhibition on response gain in the synchronous regime **(C)** Same as (B), but for the asynchronous regime (identical to Fig. 2F, replotted here for better comparison).

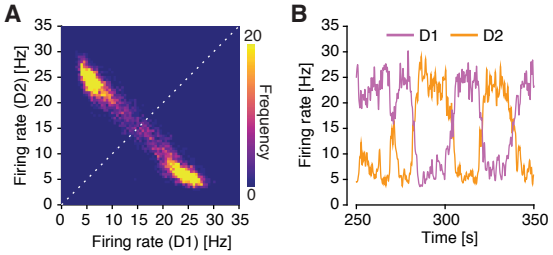

Fig. S11. Dynamics of local decision circuit under ambiguous input.
(A) With sufficient levels of background input, the network fluctuates between one of two attractor states, reflecting decision 1 or decision 2. **(B)** Temporal evolution of the activity in population D1 and D2. Perceptual transitions were defined as the time points where one population becomes dominant over the other (e.g. D1>D2).

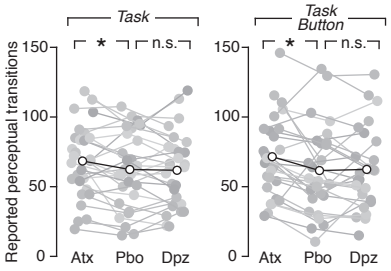

Fig. S12. Behavior during task and task-pressing
Left: Number of reported perceptual transitions after the administration of atomoxetine (Atx), placebo (Pbo) or donepezil (Dpz), separately for task (silent counting of perceptual transitions). Right: same for task-button (perceptual transitions reported through pressing a button; right) (*) indicates $P < 0.05$ (two-sided paired t-test).

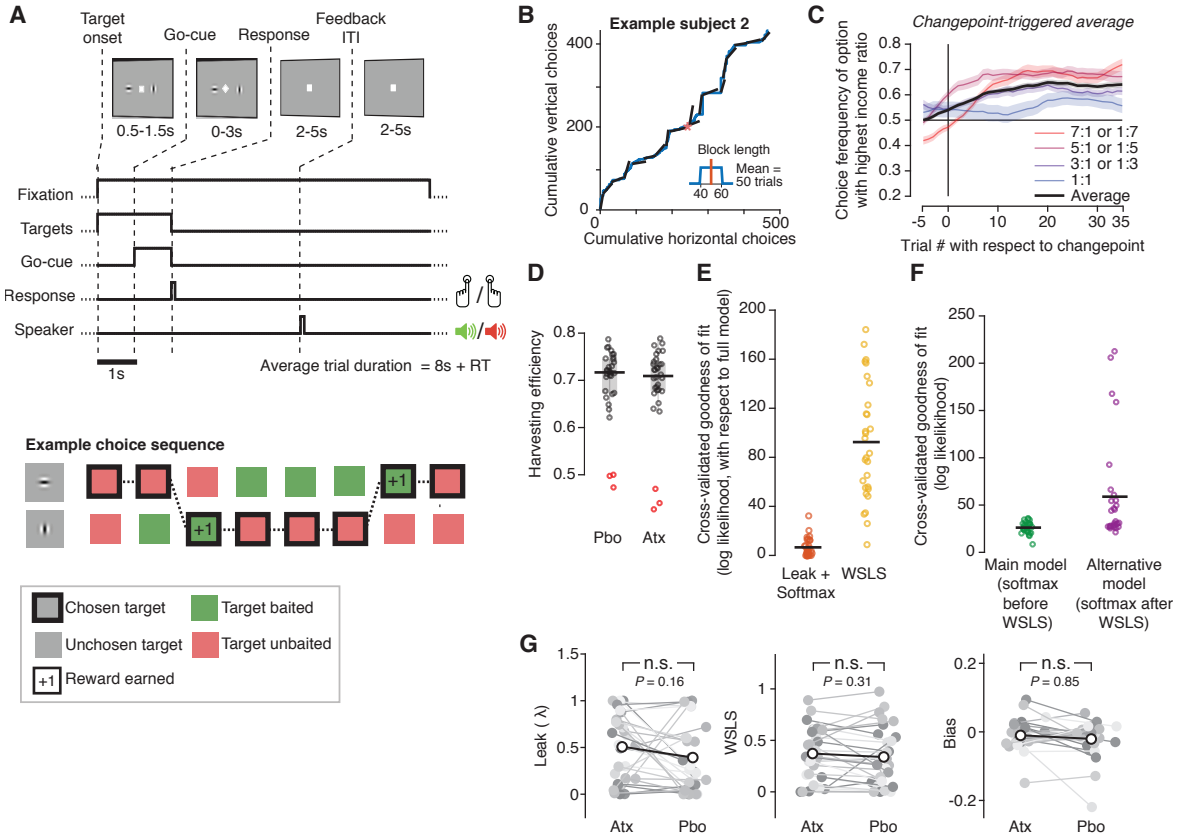

Fig. S13. Experimental design, choice behavior, and behavioral modeling for dynamic foraging task.
(A) Behavioral task. Top: sequence of events during each trial. Two choice targets (vertical/horizontal Gabor patches), associated with different reward histories and randomized by position, are presented at trial onset. A go-cue (change of fixation marker) instructs subjects to indicate their choice, by pressing a button with left or right index finger. Binary auditory feedback (reward or no-reward) is delivered after variable delay. Bottom: reward scheme as in (*29*) except that no change-over-delay was imposed (see Materials and Methods). **(B)** Dynamic foraging behavior of an example subject during a single session. Continuous blue curve, cumulative choices of horizontal vs. vertical targets. Black lines show average ratio of incomes earned from both targets (horizonzal:vertical) within each block (here, 1:5, 1:1, 3:1, 1:3, 7:1, 5:1, 1:1, 1:7, 5:1, 3:1, 1:5, 1:7, 3:1, 1:3, 1:5, 1:1, 7:1, 5:1, 1:1). **(C)** Change-point triggered change in choice fraction. **(D)** Harvesting efficiency per subject and experimental session. Harvesting efficiency was defined as fraction of collected rewards over the total number of available rewards. Red dots highlight the excluded subjects. **(E)** Cross-validated comparison between behavioral model from main Fig. 3E with a model entailing only WSLS or only reward integration. The combined model from Fig. 3E fits the data best**.** **(F)** Cross-validated comparison between behavioral model from main Fig. 3E and a model, in which non-linear (softmax) transformation of choice probability is applied after combination with WSLS heuristic. The combined model from Fig. 3E fits the data better**.** **(G)** Effects of atomoxetine on all model parameters except for decision noise (1/β) (compare Fig. 3F).

Table S1. List of included AAL regions.

REGION INDEX	AAL REGION NAME	REGION INDEX	AAL REGION NAME
1	Precentral_L	**39**	Temporal_Inf_R
2	Frontal_Sup_L	**40**	Temporal_Pole_Mid_R
3	Frontal_Sup_Orb_L	**41**	Temporal_Mid_R
4	Frontal_Mid_L	**42**	Temporal_Pole_Sup_R
5	Frontal_Mid_Orb_L	**43**	Temporal_Sub_R
6	Frontal_Inf_Oper_L	**44**	Heschl_R
7	Frontal_Inf_Tri_L	**45**	Paracentral_Lobule_R
8	Frontal_Inf_Orb_L	**46**	Precuneus_R
9	Rolandic_Oper_L	**47**	Angular_R
10	Supp_Motor_Area_L	**48**	SupraMarginal_R
11	Frontal_Supp_Medial_L	**49**	Parietal_Inf_R
12	Frontal_Med_Orb_L	**50**	Parietal_Sup_R
13	Rectus_L	**51**	Postcentral_R
14	Cingulum_Ant_L	**52**	Fusiform_R
15	Cingulum_Mid_L	**53**	Occipital_Inf_R
16	Cingulum_Post_L	**54**	Occipital_Mid_R
17	Hippocampus_L	**55**	Occipital_Sup_R
18	ParaHippocampal L	**56**	Lingual_R
19	Calcarine_L	**57**	Cuneus_R
20	Cuneus_L	**58**	Calcarine_R
21	Lingual_L	**59**	ParaHippocampal_R
22	Occipital_Sup_L	**60**	Hippocampus_R
23	Occipital_Mid_L	**61**	Cingulum_Post_R
24	Occipital_Inf_L	**62**	Cingulum_Mid_R
25	Fusiform_L	**63**	Cingulum_Ant_R
26	Postcentral_L	**64**	Rectus_R
27	Parietal_Sup_L	**65**	Frontal_Med_Orb_R
28	Parietal_Inf_L	**66**	Frontal_Supp_Medial_R
29	SupraMarginal_L	**67**	Supp_Motor_Area__
30	Angular_L	**68**	Rolandic_Oper_R
31	Precuneus_L	**69**	Frontal_Inf_Orb_R
32	Paracentral_Lobule_L	**70**	Frontal_Inf_Tri_R
33	Heschl_L	**71**	Frontal_Inf_Oper_R
34	Temporal_Sub_L	**72**	Frontal_Mid_Orb_R
35	Temporal_Pole_Sup_L	**73**	Frontal_Mid_R
36	Temporal_Mid_L	**74**	Frontal_Sup_Orb_R
37	Temporal_Pole_Mid_L	**75**	Frontal_Sup_R
38	Temporal_Inf_L	**76**	Precentral_R

List of cortical AAL regions included in the model-based analysis.

Movie S1. 3D-Structure-from-motion stimulus.
https://www.youtube.com/watch?v=baZqACCbQqk

The 3D-Structure-from-Motion stimulus presented to the participants during Task.